INTERNATIONAL JOURNAL FOR NUMERICAL METHODS IN FLUIDS
Int. J. Numer. Meth. Fluids **31**: 821–860 (1999)

A CFD EULER SOLVER FROM A PHYSICAL ACOUSTICS–CONVECTION FLUX JACOBIAN DECOMPOSITION

JOE IANNELLI*

Department of Mechanical and Aerospace Engineering and Engineering Science, The University of Tennessee, 315 Perkins Hall, Knoxville TN 3799-2030, USA

SUMMARY

This paper introduces a continuum, i.e. non-discrete, upstream-bias formulation that rests on the physics and mathematics of acoustics and convection. The formulation induces the upstream-bias at the differential equation level, within a characteristics-bias system associated with the Euler equations with general equilibrium equations of state. For low subsonic Mach numbers, this formulation returns a consistent upstream-bias approximation for the non-linear acoustics equations. For supersonic Mach numbers, the formulation smoothly becomes an upstream-bias approximation of the entire Euler flux. With the objective of minimizing induced artificial diffusion, the formulation non-linearly induces upstream-bias, essentially locally, in regions of solution discontinuities, whereas it decreases the upstream-bias in regions of solution smoothness. The discrete equations originate from a finite element discretization of the characteristic-bias system and are integrated in time within a compact block tridiagonal matrix statement by way of an implicit non-linearly stable Runge–Kutta algorithm for stiff systems. As documented by several computational results that reflect available exact solutions, the acoustics–convection solver induces low artificial diffusion and generates essentially non-oscillatory solutions that automatically preserve a constant enthalpy, as well as smoothness of both enthalpy and mass flux across normal shocks. Copyright © 1999 John Wiley & Sons, Ltd.

KEY WORDS: CFD; upwind; artificial diffusion; acoustics; convection; finite elements; implicit integration

1. INTRODUCTION

This paper introduces for the Euler equations, with general equilibrium equations of state, a stable and consistent upstream-bias algorithm that rests on a new flux Jacobian decomposition (FJD) formulation, features the simplicity of a flux vector splitting formulation and accommodates an implicit solver. The algorithm induces minimal diffusion, naturally incorporates a finite element discretization and uniquely generates the upstream-bias directly at the differential equation level before and independently of any discrete approximation on specified grids. As one of its important features, the algorithm combines the mathematics of upwind algorithms with the physics of acoustics and convection, the wave propagation mechanisms within gas dynamic flows.

* Correspondence to: Department of Mechanical and Aerospace Engineering and Engineering Science, The University of Tennessee, 315 Perkins Hall, Knoxville TN 3799-2030, USA. E-mail: jiannell@utk.edu

CCC 0271–2091/99/210821–40$17.50

Received January 1998
Revised March 1998

Most finite element, difference and volume algorithms have remained largely independent from the physics of acoustics and convection. The dissipation mechanisms within these algorithms, furthermore, have been developed at the discrete level in connection with a specific grid.

Several finite element Euler solvers have either utilized modifications of the test space, e.g. SUPG [1], or introduced Taylor's series-based dissipation terms, e.g. TWS [2], to generate stable algorithms. The mathematical developments in these fundamental contributions have remained independent from characteristics theory.

Most characteristic upwind schemes have been implemented through finite difference and finite volume discrete approximations [3]. Roe's approximate Riemann solver [4] remains an upwind procedure with a significant physics content. The associated operation count, on the other hand, exceeds that of a flux vector splitting formulation.

VanLeer's original simple flux vector splitting, and the many variants developed thereafter [5], essentially rely on Mach number dependent polynomials to generate flux components, each featuring Jacobian eigenvalues with uniform algebraic signs. As such, these fundamental mathematical developments remain independent from the physics of acoustics and convection.

As a spin-off from these studies and presented as a new perfect-gas flux vector splitting, Liou and Steffen's procedure [6] employs an *ad hoc* advection velocity along with flux components with convection and pressure physical meanings. An analogous method was introduced earlier by this author [7] and the essentially non-oscillatory results from both methods bear out the advantages of employing flux components with clear physical significance.

The eigenvalues of the various convection and pressure fluxes in these methods, however, either approach zero or remain substantially less than the speed of sound for decreasing Mach number. Neither method has, therefore, generated a physically consistent upstream-bias approximation of the acoustics limit of the Euler equations in the low-Mach number regime. In fact no single decomposition of the Euler flux contains separate components that respectively correspond to the physics of acoustics and convection.

In this paper, a new upstream-bias formulation is developed that is based on a decomposition of the Euler flux vector Jacobian into matrix components. This formulation encompasses, unifies and generalizes upwind algorithms, including flux vector splitting and flux difference splitting developments. This formulation develops the upstream-bias approximation directly at the differential equation level, before any discretization. The method results in a 'companion' characteristics-bias system that is associated with the Euler equations and contains an upstream-bias differential expression. The characteristics-bias system features a characteristics flux that generalizes, in the continuum, the traditional numerical fluxes of upwind schemes. The acoustic–convection upstream algorithm then results from a specific decomposition of the flux vector Jacobian into genuine acoustics and convection components, for a physically consistent upstream approximation of coupled acoustic and convection wave propagation.

A traditional centered discretization of the acoustics–convection characteristics-bias system then automatically generates a coherent upstream discrete approximation of the governing Euler equations. This approximation, moreover, reduces to a consistent upstream approximation of the acoustics equations, for vanishing Mach number, which addresses the challenging problem of calculating low-Mach number flows. Finite difference, volume or element procedures can be used to discretize the characteristics-bias system. The algorithm in this paper has used a finite element discretization, which also leads naturally and automatically to consistent boundary differential equations and a new outlet pressure boundary condition that does not require any algebraic extrapolation of variables. The resulting discrete equations correspond to

an essentially centered discretization in the form of a non-linear combination of upstream diffusive and downstream antidiffusive flux differences, with greater bias on the upstream diffusive flux difference. This formulation, furthermore, directly accommodates an implicit solver, for it is very easy to determine the required Jacobian matrices.

With the objective of minimizing induced artificial diffusion, the characteristics-bias flux non-linearly induces upstream-bias essentially locally in regions of solution discontinuities, whereas it decreases the upstream-bias in regions of solution smoothness. This variable diffusion is automatically adjusted at each discretization node by a new controller, also introduced in this paper. This controller depends on local solution slope jumps and varies the combination weights on the upstream and downstream fluxes, within the discrete equations.

The operation count for this algorithm is comparable with that of a simple flux vector splitting algorithm. The developments in this study have employed basic two-noded cells, which has thus led to a block tridiagonal matrix system, for the implicit formulation. To determine the ultimate accuracy of linear approximations of fluxes within two-noded cells, for a computationally efficient implementation, this study employs no MUSCL-type local extrapolation of dependent variables.

This paper is organized into nine sections. After the introductory remarks in Section 1, Section 2 presents the governing equations and Sections 3 develops the flux Jacobian decomposition formulation. Section 4 presents the decomposition of the Euler flux Jacobian into genuinely physical acoustic and convection components, followed in Section 5 by the determination of the corresponding upstream-bias stability eigenvalues. Section 6 details the finite element spatial discretization, along with the new pressure boundary condition and solution dependent control of upstream diffusion, and Section 7 delineates the non-linearly stable implicit Runge–Kutta time integration. The computational results are discussed in Section 8, with concluding remarks presented in Section 9.

2. GOVERNING EQUATIONS

2.1. Euler system

With respect to an inertial reference frame, the quasi-one-dimensional Euler conservation law system [3] is:

$$\frac{\partial q}{\partial t}+\frac{\partial f(q)}{\partial x}=\phi, \tag{1}$$

where the independent variable (x, t) varies in the domain $D \equiv \Omega \times [t_0, T]$, $\Omega \equiv [a, b]$. This system consists of the continuity, momentum and total energy equations, and the arrays $q = q(x, t)$, $f = f(q)$ and $\phi = \phi(x, q)$ are defined as

$$q \equiv \begin{Bmatrix} \rho \\ m \\ E \end{Bmatrix}, \qquad f(q) \equiv \begin{Bmatrix} m \\ \dfrac{m^2}{\rho}+p \\ \dfrac{m^2}{\rho}(E+p) \end{Bmatrix}, \qquad \phi \equiv -\frac{m}{\rho A/A_*}\frac{\mathrm{d}A/A_*}{\mathrm{d}x}\begin{Bmatrix} \rho \\ m \\ E+p \end{Bmatrix}, \tag{2}$$

where ρ, m and E respectively denote static density and volume-specific linear momentum and total energy; the Eulerian flow velocity u is then defined as $u \equiv m/\rho$. The terms p, $A = A(x)$ and A_* respectively indicate static pressure, area of the flow duct cross-section and constant upstream-flow reference throat area.

2.2. Equilibrium equation of state, pressure derivatives, speed of sound

For any homogeneous equilibrium gas, pressure depends upon two other thermodynamic variables [8]. They are density ρ and mass specific internal energy ϵ, in this case, since they are readily available from the Euler system (1): ρ directly from the continuity equation in the system, and ϵ from q as

$$\epsilon \equiv \frac{E}{\rho} = \frac{1}{2\rho^2} m^2. \tag{3}$$

The pressure equation of state thus becomes

$$p = p(\rho, \epsilon) = p\left(\rho, \frac{E}{\rho} - \frac{1}{2\rho^2} m^2\right). \tag{4}$$

The Jacobian derivatives of p with respect to q, for the Jacobian $\partial f/\partial q$ of $f(q)$, are not all independent of one another. The derivatives of (4) with respect to m and E in fact satisfy the constraint

$$\left.\frac{\partial p}{\partial m}\right|_{\rho,E} = -\frac{m}{\rho}\left.\frac{\partial p}{\partial E}\right|_{\rho,m}, \tag{5}$$

as obtained by expressing the derivatives of p with respect to m and E in terms of the thermodynamic derivative of p with respect to ϵ, from the first expression in (4). In the following sections, for simplicity, the abridged notation

$$p_\rho \equiv \left.\frac{\partial p}{\partial \rho}\right|_{m,E}, \qquad p_m \equiv \left.\frac{\partial p}{\partial m}\right|_{\rho,E}, \qquad p_E \equiv \left.\frac{\partial p}{\partial E}\right|_{\rho,m}, \tag{6}$$

will denote the Jacobian derivatives of pressure. The particular perfect-gas expressions for (4) follow from the internal energy and equation of state

$$\epsilon = c_v T = \frac{R}{\gamma - 1} T, \qquad p = \rho R T \tag{7}$$

for this type of gas, where c_v, T, R and γ respectively denote the constant-volume specific heat, static temperature, gas constant and specific-heat ratio. The elimination of T from these two expressions and use of (3) leads to the following familiar expressions for the equation of state for p in terms of q

$$p = (\gamma - 1)\rho\epsilon = (\gamma - 1)\left(E - \frac{1}{2\rho} m^2\right). \tag{8}$$

The square of the speed of sound c for general equilibrium equations of state can be expressed [9] as

$$c^2 \equiv \left.\frac{\partial p}{\partial \rho}\right|_S = p_\rho + p_E\left(\frac{E+p}{\rho} - \frac{m^2}{\rho^2}\right), \tag{9}$$

in terms of the Jacobian partial derivatives of p. With this result, the mass specific total enthalpy H depends on q as

$$H \equiv \frac{E+p}{\rho} = \frac{1}{p_E}(c^2(1+p_E M^2) - p_\rho), \tag{10}$$

where $M \equiv \|u\|/c$ denotes the Mach number.

2.3. Characteristics analysis

For general equilibrium pressure equations of state (4), the characteristic speeds associated with the Euler equations, i.e. the eigenvalues of the flux vector Jacobian

$$\frac{\partial f(q)}{\partial q} = \begin{pmatrix} 0 & 1 & 0 \\ -\dfrac{m^2}{\rho^2} + p_\rho & \dfrac{2m}{\rho} + p_m & p_E \\ -\dfrac{m}{\rho^2}(E+p) + \dfrac{m}{\rho} p_\rho & \dfrac{E+p}{\rho} + \dfrac{m}{\rho} p_m & \dfrac{m}{\rho}(1+p_E) \end{pmatrix} \tag{11}$$

have been exactly determined in closed form as

$$\lambda_1 = u, \qquad \lambda_{2,3} = u \pm \left(p_\rho + p_E \left(\frac{E+p}{\rho} - \frac{m^2}{\rho^2} \right) \right)^{1/2}. \tag{12}$$

These eigenvalues correspond to the slopes of the characteristics, as portrayed in Figure 1 for representative hypersonic, supersonic, sonic and subsonic flows.

Of interest, eigenvalues $\lambda_{2,3}$ directly incorporate a sound speed expression that coincides with the isentropic partial derivative of pressure (9). Through (9), therefore, these equilibrium-gas eigenvalues become

$$\lambda_1^E = u, \qquad \lambda_{2,3}^E = u \pm c, \tag{13}$$

which have the same familiar form as the perfect gas eigenvalues.

Figure 1 shows the characteristics in a suitable neighborhood of a flow field point P in a (t, x)-plane. An interesting geometric difference among supersonic, sonic and subsonic flows is that a time axis through P is respectively outside, on the boundary and inside the domain of dependence and range of influence of point P. Wave propagation for supersonic flows essentially occurs by convection, monoaxially from upstream to downstream of P; the sonic case becomes a limiting case; for subsonic flows, instead, wave propagation occurs by both convection and acoustics, bimodally from both upstream and downstream toward P; for vanishing Mach number, wave propagation is essentially acoustic.

Since gas dynamic wave propagation physically occurs by acoustics and convection, the upstream CFD algorithm in this paper mathematically models this coupled acoustic–convection wave propagation. The algorithm identifies the genuine convection and acoustics components within the flux Jacobian and then establishes a physically consistent upstream approximation for each of these components.

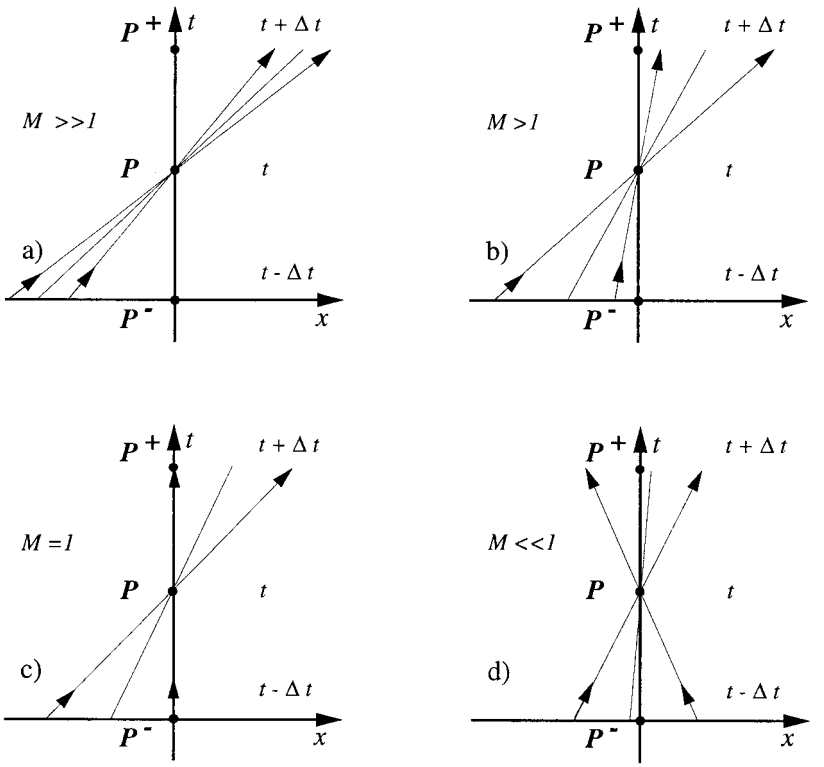

Figure 1. Characteristics: (a) hypersonic, (b) supersonic, (c) sonic, (d) subsonic.

2.4. Non-linear acoustics equations

The Euler equations contain the acoustics equations for vanishing Mach numbers. Identification of these equations yields the acoustics component of the Euler flux Jacobian for any Mach number. Upon writing momentum m in terms of the Mach number M as $m = \rho c M u/|u|$ and using the energy pressure derivative identity (5), the Euler system (1) becomes

$$\begin{aligned}
&\frac{\partial \rho}{\partial t} + \frac{\partial m}{\partial x} + cM \frac{u}{|u|} \frac{\rho}{A} \frac{\mathrm{d}A}{\mathrm{d}x} = 0,\\
&\frac{\partial m}{\partial t} + p_\rho \frac{\partial \rho}{\partial x} + p_E \frac{\partial E}{\partial x} + cM \frac{u}{|u|} \left[(2 - p_E) \frac{\partial m}{\partial x} - \frac{m}{\rho} \frac{\partial \rho}{\partial x} + \frac{m}{A} \frac{\mathrm{d}A}{\mathrm{d}x} \right] = 0,\\
&\frac{\partial E}{\partial t} + \frac{E+p}{\rho} \frac{\partial m}{\partial x} + cM \frac{u}{|u|} \left[\rho \frac{\partial}{\partial x} \left(\frac{E+p}{\rho} \right) + \frac{E+p}{A} \frac{\mathrm{d}A}{\mathrm{d}x} \right] = 0,
\end{aligned} \tag{14}$$

and for a vanishing Mach number, these equations reduce to the non-linear acoustics system

$$\frac{\partial}{\partial t} \begin{pmatrix} \rho \\ m \\ E \end{pmatrix} + \begin{pmatrix} 0 & 1 & 0 \\ p_\rho & 0 & p_E \\ 0 & \dfrac{E+p}{\rho} & 0 \end{pmatrix} \frac{\partial}{\partial x} \begin{pmatrix} \rho \\ m \\ E \end{pmatrix} = 0 \Rightarrow \frac{\partial q}{\partial t} + A^{a_0} \frac{\partial q}{\partial x} = 0, \tag{15}$$

where A^{a_0} denotes the zero Mach number acoustics matrix. The dependent variables in these equations correspond to those in a flow field that originates from slight perturbations to an otherwise quiescent field.

Heed that the energy equation toward steady state, in this case, is no longer linearly independent from the continuity equation. This phenomenon directly explains the widely reported convergence difficulties experienced in the CFD simulation of incompressible, i.e. low Mach number, flows with a compressible flow formulation.

By virtue of the total enthalpy expression (10), the matrix A^{a_0} becomes

$$A^{a_0} = \begin{pmatrix} 0 & 1 & 0 \\ p_\rho & 0 & p_E \\ 0 & \dfrac{c^2 - p_\rho}{p_E} & 0 \end{pmatrix}, \tag{16}$$

with eigenvalues

$$\lambda_1^{a_0} = 0, \qquad \lambda_{2,3}^{a_0} = \pm c. \tag{17}$$

where c corresponds to the zero-Mach number isentropic speed of sound (9). With $\lambda_1^{a_0} = 0$, the propagation of (acoustic) waves governed by this system, therefore, corresponds to an isentropic process with negligible flow kinetic energy.

Equations (15) contain the important expressions

$$\frac{\partial E}{\partial x} = \frac{c^2 - p_\rho}{p_E}\frac{\partial \rho}{\partial x}, \qquad \frac{\partial \rho}{\partial x}\frac{p_E}{c^2 - p_\rho}\frac{\partial E}{\partial x}, \tag{18}$$

which result from the momentum equation by expressing p_ρ therein using (9) as

$$\begin{aligned} \frac{\partial m}{\partial t} &= -\frac{\partial p}{\partial x} = -p_\rho \frac{\partial \rho}{\partial x} - p_E \frac{\partial E}{\partial x} = -\left(\frac{\partial p}{\partial \rho}\bigg|_S - p_E \frac{E+p}{\rho}\right)\frac{\partial \rho}{\partial x} - p_E \frac{\partial E}{\partial x} \\ &= -\frac{\partial p}{\partial \rho}\bigg|_S \frac{\partial \rho}{\partial x} - p_E\left(\frac{\partial E}{\partial x} - \frac{E+p}{\rho}\frac{\partial \rho}{\partial x}\right). \end{aligned} \tag{19}$$

For an isentropic flow $p = p(\rho)$, hence the first right-hand-side term in (19) equals $\partial p/\partial x$. The second right-hand-side term must consequently vanish, which returns results (18), after using (10). These results will conveniently simplify the acoustics–convection upstream formulation in Sections 4.2 and 4.3.

3. NON-DISCRETE UPSTREAM-BIAS APPROXIMATION

The non-discrete, i.e. continuum or before discretization, upstream-bias approximation of the Euler equations derives from a characteristics-bias integral statement associated with (1). The prototype integral statement is

$$\int_{\hat{\Omega}} \hat{w}\left(\frac{\partial q}{\partial t} - \phi + \frac{\partial f(q)}{\partial x}\right) \mathrm{d}\Omega = 0, \tag{20}$$

which is equivalent to the governing system (1) for arbitrary subdomains $\hat{\Omega} \subset \Omega$ and arbitrary test functions with compact support in $\hat{\Omega}$. The characteristic-bias integral is then defined as

$$\int_{\hat{\Omega}} \hat{w}\left(\frac{\partial q}{\partial t} - \phi + \frac{\partial f^{\mathrm{C}}}{\partial x}\right) \mathrm{d}\Omega = 0, \tag{21}$$

where f^{C} corresponds to a characteristic-bias flux that automatically induces within (21) an upstream-bias approximation for the Euler flux divergence $\partial f/\partial x$.

3.1. Flux Jacobian decomposition and upstream-bias integral average

To develop the flux f^{C} consider first the flux Jacobian decomposition (FJD) into L contributions

$$\frac{\partial f}{\partial q} = \sum_{\ell=1}^{L} \alpha_\ell A_\ell \Rightarrow \frac{\partial f}{\partial x} = \sum_{\ell=1}^{L} \alpha_\ell A_\ell \frac{\partial q}{\partial x}, \tag{22}$$

where A_ℓ corresponds to a flux-Jacobian matrix component with uniform-sign eigenvalues and α_ℓ denotes a linear combination function, possibly depending upon q.

An integral average of the Euler flux divergence $\partial f/\partial x$ as expressed through decomposition (22) becomes

$$\int_{\hat{\Omega}} \hat{w} \frac{\partial f}{\partial x} \mathrm{d}\Omega = \int_{\hat{\Omega}} \sum_{\ell=1}^{L} \hat{w}\alpha_\ell A_\ell \frac{\partial q}{\partial x} \mathrm{d}\Omega. \tag{23}$$

The flux f^{C} is therefore defined by way of an upstream-bias integral average as

$$\int_{\hat{\Omega}} \hat{w} \frac{\partial f^{\mathrm{C}}}{\partial x} \mathrm{d}\Omega = \int_{\hat{\Omega}} \sum_{\ell=1}^{L} (\hat{w} + \psi\delta_\ell \hat{w})\alpha_\ell A_\ell \frac{\partial q}{\partial x} \mathrm{d}\Omega, \tag{24}$$

where the right-hand-side integral provides an upstream-bias for each matrix component within the FJD in (22).

The positive ψ in (24), $0 < \psi < 1$, stands for a new 'upstream-bias' controller, which automatically adjusts the amount of induced upstream-bias diffusion, depending on local solution non-smoothness, as introduced and detailed in Section 6.3. The variation $\delta_\ell \hat{w}$ induces the appropriate upstream-bias for the test function $\hat{w}$ for each 'ℓ' component within (24). Depending on the physical significance, magnitude and algebraic sign of the eigenvalues of A_ℓ, the variation $\delta_\ell \hat{w}$ can vanish or become algebraically positive or negative, which corresponds to an upstream-bias respectively in the negative or positive sense of the x-axis.

3.2. Characteristics-bias flux

The variation $\delta_\ell \hat{w}$ in (24) becomes

$$\delta_\ell \hat{w} = \frac{\partial \hat{w}}{\partial x} \delta_\ell x = \frac{\partial \hat{w}}{\partial x} a_\ell \varepsilon, \quad a_\ell \varepsilon = \delta_\ell x, \tag{25}$$

where ε denotes a local positive length scale, while the direction cosine a_ℓ can equal 0 or $+1$, -1, possibly also depending upon q.

With these specifications, the upstream-bias integral average (24) becomes

$$\int_{\hat{\Omega}} \hat{w} \frac{\partial f^{\mathrm{C}}}{\partial x} \mathrm{d}\Omega = \int_{\hat{\Omega}} \hat{w} \frac{\partial f}{\partial x} \mathrm{d}\Omega + \int_{\hat{\Omega}} \varepsilon\psi \frac{\partial \hat{w}}{\partial x} \sum_{\ell=1}^{L} a_\ell \alpha_\ell A_\ell \frac{\partial q}{\partial x} \mathrm{d}\Omega. \tag{26}$$

Considering that $\hat{w}$ has compact support in $\hat{\Omega}$, it vanishes on the boundary $\partial\hat{\Omega}$ of $\hat{\Omega}$. As a result, integrating (26) by parts generates

$$\int_{\hat{\Omega}} \hat{w}\left[\frac{\partial f^{\mathrm{C}}}{\partial x}-\frac{\partial f}{\partial x}+\frac{\partial}{\partial x}\left(\varepsilon\psi \sum_{\ell=1}^{L} a_\ell \alpha_\ell A_\ell \frac{\partial q}{\partial x}\right)\right] \mathrm{d}\Omega = 0, \tag{27}$$

which contains no boundary integrals. Since this integral must vanish for arbitrary test functions $\hat{w}$ and domains $\hat{\Omega}$, its integrand must equal zero, which generates the following expression for the divergence of the characteristics-bias flux f^C

$$\frac{\partial f^{\mathrm{C}}}{\partial x}=\frac{\partial f}{\partial x}-\frac{\partial}{\partial x}\left(\varepsilon\psi \sum_{\ell=1}^{L} a_\ell \alpha_\ell A_\ell \frac{\partial q}{\partial x}\right). \tag{28}$$

This expression exhibits an upstream-bias artificial diffusion, in the form of a second-order differential expression with matrix

$$\mathscr{A} \equiv \sum_{\ell=l}^{L} a_\ell \alpha_\ell A_\ell. \tag{29}$$

For physical consistency of the upstream bias in (24)–(28) and associated mathematical stability of the corresponding second-order differential expression, all the eigenvalues of this upstream matrix must be positive. This requirement becomes a fundamental upstream-bias stability condition.

For two- and three-dimensional flows, and with implied summation on repeated indices, the version of the characteristics-bias flux follows as a multi-dimensional generalization of (22)–(29) as

$$\frac{\partial f_i}{\partial x_j}=\sum_{\ell=1}^{L} \alpha_\ell A_{\ell j} \frac{\partial q}{\partial x_j}, \qquad \delta_\ell \hat{w}=\frac{\partial \hat{w}}{\partial x_j}\delta_\ell x_j=\frac{\partial \hat{w}}{\partial x_j}a_{j\ell}\varepsilon \tag{30}$$

and

$$\frac{\partial f_j^{\mathrm{C}}}{\partial x_j}=\frac{\partial f_j}{\partial x_j}-\frac{\partial}{\partial x_i}\left(\varepsilon\psi \sum_{\ell=1}^{L} a_{i\ell}\alpha_\ell A_{\ell j}\frac{\partial q}{\partial x_j}\right), \qquad \mathscr{A} \equiv \omega_i\left(\sum_{\ell=1}^{L} a_{i\ell}\alpha_\ell A_{\ell j}\right)\omega_j, \tag{31}$$

with $1 \le i, j \le 2$ for two-dimensional, and $1 \le i, j \le 3$ for three-dimensional flows. In these expressions, $a_{i\ell}$ now denotes the ith direction cosine of a unit vector $\boldsymbol{a}_\ell$ along the principal wave propagation direction of wave 'ℓ' and ω_i indicates the ith direction cosine of a unit vector $\boldsymbol{\omega}$ along an arbitrary wave propagation direction. The multi-dimensional acoustics–convection form of (31) is being completed, but will be detailed soon in a companion paper, to keep the length of each of these two papers within an appropriate size.

The continuum expression (28), or (31), for the divergence of the characteristics-bias flux constitutes a non-discrete generalization of the various numerical flux formulae employed in several CFD upwind schemes. It encompasses, generalizes and unifies flux vector and flux difference schemes as shown by the following representative examples.

3.2.1. van Leer's formulation and flux vector splitting. Consider the van Leer formulation as a representative flux vector splitting (FVS). In this formulation, the inviscid flux f is 'split' as

$$f=f^{\mathrm{VL}^+}+f^{\mathrm{VL}^-}, \tag{32}$$

where the Jacobian matrices of f^{VL^+} and f^{VL^-} respectively possess non-negative and non-positive eigenvalues.

The FJD expression (22) encompasses (32) with $L=2$ as

$$\sum_{\ell=1}^{L} \alpha_\ell A_\ell=\frac{\partial f^{\mathrm{VL}^+}}{\partial q}+\frac{\partial f^{\mathrm{VL}^-}}{\partial q}, \quad \alpha_1=1, \quad \alpha_2=1. \tag{33}$$

The corresponding characteristics-bias flux divergence for van Leer's FVS accrues from (28) with $\psi = 1,\ a_1 = 1,\ a_2 = -1$ as

$$\frac{\partial f^{\mathrm{C}}}{\partial x} = \frac{\partial f}{\partial x} - \frac{\partial}{\partial x}\left(\varepsilon\left(\frac{\partial f^{\mathrm{VL}^+}}{\partial q} - \frac{\partial f^{\mathrm{VL}^-}}{\partial q}\right)\frac{\partial q}{\partial x}\right) = \frac{\partial f}{\partial x} - \frac{\partial}{\partial x}\left(\varepsilon\left(\frac{\partial f^{\mathrm{VL}^+}}{\partial x} - \frac{\partial f^{\mathrm{VL}^-}}{\partial x}\right)\right), \tag{34}$$

which generalizes, in the continuum, the traditional numerical flux formulae for FVS constructions.

The associated upstream matrix $\mathscr{A}$ is

$$\mathscr{A} = \frac{\partial f^{\mathrm{VL}^+}}{\partial q} - \frac{\partial f^{\mathrm{VL}^-}}{\partial q}. \tag{35}$$

The upstream-bias stability condition, however, is not automatically satisfied, even though each of the two matrices $(\partial f^{\mathrm{VL}^+}/\partial q)$ and $(-\partial f^{\mathrm{VL}^-}/\partial q)$ has positive eigenvalues. This stability condition is not unconditionally satisfied because the sum of two positive-eigenvalue matrices does not necessarily yield a matrix with positive eigenvalues. As an example, consider the following matrix sum of two positive-eigenvalue matrices

$$\begin{pmatrix} 2 & \sigma \\ 3 & 6 \end{pmatrix} = \begin{pmatrix} 1 & 0 \\ 3 & 2 \end{pmatrix} + \begin{pmatrix} 1 & \sigma \\ 0 & 4 \end{pmatrix}, \tag{36}$$

where σ is a real number. One of the eigenvalues of this matrix sum is negative for $\sigma > 4$. For instance, for $\sigma = 7$, the eigenvalues are $+9$ and -1.

Most likely, however, (35) satisfies the upstream-bias stability condition for most of the flow conditions considered in the technical literature, in view of the stable results reported. For subsonic flows, each of the two flux vector components in (32) remains unrelated to the physics of acoustics or convection. On the other hand, (32) is computationally advantageous, for it calls for the discretization of simple flux vector components.

3.2.2. Roe's formulation and flux difference splitting. Consider next Roe's formulation as a representative flux difference splitting (FDS) development. In this formulation, the inviscid flux Jacobian of f is 'split' as

$$\frac{\partial f}{\partial q} = X\Lambda^+ X^{-1} + X\Lambda^- X^{-1}, \tag{37}$$

where X and $\Lambda = \Lambda^+ + \Lambda^-$ denote the right eigenvector matrix and eigenvalue diagonal matrix of the Jacobian, all evaluated at special average values of q, with Λ^+ and Λ^- respectively containing non-negative and non-positive eigenvalues. The matrices on the right-hand-side of (37), therefore, will respectively possess non-negative and non-positive eigenvalues.

The FJD expression (22) encompasses (37) with $L = 2$ as

$$\sum_{\ell=1}^{L} \alpha_\ell A_\ell = X\Lambda^+ X^{-1} + X\Lambda^- X^{-1}, \quad \alpha_1 = 1, \quad \alpha_2 = 1. \tag{38}$$

The corresponding characteristics-bias divergence for Roe's formulation accrues from (28) with $\psi = 1,\ a_1 = 1,\ a_2 = -1$ as

$$\frac{\partial f^{\mathrm{C}}}{\partial x} = \frac{\partial f}{\partial x} - \frac{\partial}{\partial x}\left(\varepsilon(X\Lambda^+ X^{-1} - X\Lambda^- X^{-1})\frac{\partial q}{\partial x}\right) = \frac{\partial f}{\partial x} - \frac{\partial}{\partial x}\left(\varepsilon X(\Lambda^+ - \Lambda^-)X^{-1}\frac{\partial q}{\partial x}\right), \tag{39}$$

which generalizes in the continuum the traditional numerical flux formulae for FDS constructions.

The associated upstream matrix $\mathscr{A}$ is

$$\mathscr{A} = X(\Lambda^+ - \Lambda^-)X^{-1}, \tag{40}$$

which has non-negative eigenvalues, and therefore automatically satisfies the upstream-bias stability condition for any flow state for which no eigenvalue vanishes. The discretization of (39) calls for more computational operations than (34), while each of the two right-hand-side components in (37) lumps into one matrix the matrices representative of the distinct acoustics and convection wave propagation mechanisms. On the other hand, numerous numerical results bear out the accuracy of an FDS formulation.

4. ACOUSTICS–CONVECTION FLUX JACOBIAN DECOMPOSITION

The acoustics–convection flux Jacobian decomposition consists of components that genuinely model the physics of acoustics and convection. These components combine the computational simplicity of FVS with the accuracy and stability of FDS and also feature eigenvalues with uniform algebraic signs. This formulation eliminates the unstable linear-dependence problem in steady low-Mach number flows and satisfies by design the upstream-bias stability condition. As the Mach number increases, the formulation smoothly approaches and then becomes an upstream-bias approximation of the entire flux divergence, along one single direction.

4.1. Convection and pressure gradient components

The flux divergence $\partial f/\partial x$ can be decomposed into convection and pressure gradient components as

$$\frac{\partial f}{\partial x} = \frac{\partial f^q}{\partial x} + \frac{\partial f^p}{\partial x}, \tag{41}$$

where f^q and f^P respectively denote the convection and pressure fluxes, defined as

$$f^q(q) \equiv \begin{Bmatrix} m \\ \dfrac{m^2}{\rho} \\ \dfrac{m}{\rho}(E+p) \end{Bmatrix} = \frac{m}{\rho} \cdot \begin{Bmatrix} \rho \\ m \\ E+p \end{Bmatrix}, \qquad f^p \equiv \begin{Bmatrix} 0 \\ p \\ 0 \end{Bmatrix}. \tag{42}$$

For supersonic flows, the Euler eigenvalues (13), associated with $\partial f/\partial x$ all have the same algebraic sign and the entire flux divergence can be upstream approximated along one single direction. For subsonic flows these eigenvalues have mixed algebraic sign and an upstream approximation for the flux divergence along one single direction remains inconsistent with the two-way propagation of acoustic waves. Without the pressure gradient in the momentum equation, however, the corresponding flux Jacobian eigenvalues all have the same algebraic sign [9] and the resulting convection flux divergence can then be upstream approximated along one single direction. The flux divergence can thus be decomposed as the linear combination

$$\frac{\partial f}{\partial x}=\left[\frac{\partial f^q}{\partial x}+\beta\frac{\partial f^p}{\partial x}\right]+\left[(1+\beta)\frac{\partial f^p}{\partial x}\right],\quad 0\le\beta\le 1, \tag{43}$$

where the positive pressure-gradient partition function β can be chosen in such a way that all the eigenvalues of each of the two components between brackets in (43) keep the same algebraic sign for all Mach numbers. In this manner, these entire components can be upstream approximated along single directions. This choice for β is possible because the eigenvalues of a matrix are continuous functions of the matrix entries [10] and hence all the eigenvalues for the components in (43) will continuously depend upon β. The function β will gradually increase toward 1 for increasing Mach numbers, so that an upstream approximation for the components in (43) smoothly approaches and then becomes an upstream approximation for the entire $\partial f/\partial x$ along one single direction. Decomposition (43) is thus used for an upstream approximation of the flux divergence for subsonic and supersonic flows.

For low and vanishing Mach numbers, decomposition (43), however, is insufficient for an accurate upstream modeling of acoustic waves. For a Mach number that approaches zero, the Euler eigenvalues (13) can all keep the same algebraic sign only if the sound speed contribution vanishes, which corresponds to a vanishing pressure gradient contribution and hence β approaching zero [9]. But for β approaching zero, the eigenvalues associated with the components in (43) approach the eigenvalues of the Jacobians

$$\frac{\partial f^q(q)}{\partial q}=\begin{pmatrix} 0 & 1 & 0 \\ -\dfrac{m^2}{\rho^2} & \dfrac{2m}{\rho} & 0 \\ -\dfrac{m^2}{\rho^2}(E+p)+\dfrac{m}{\rho}p_\rho & \dfrac{E+p}{\rho}+\dfrac{m}{\rho}p_m & \dfrac{m}{\rho}(1+p_E) \end{pmatrix} \tag{44}$$

and

$$\frac{\partial f^p}{\partial q}=\begin{pmatrix} 0 & 0 & 0 \\ p_\rho & p_m & p_E \\ 0 & 0 & 0 \end{pmatrix}. \tag{45}$$

Using the pressure derivative identity (5), the eigenvalues of these Jacobians respectively are

$$\lambda^q_{1,2}=\frac{m}{\rho},\qquad \lambda^q_3=\frac{m}{\rho}(1+p_E) \tag{46}$$

and

$$\lambda^p_{1,2}=0,\qquad \lambda^p_3=p_m=-\frac{m}{\rho}p_E, \tag{47}$$

which certainly all keep the same algebraic sign, but for vanishing Mach number remain far less than the dominant speed of sound c. For low Mach numbers, therefore, an upstream approximation for the components in (43) would inaccurately model the physics of acoustics. This difficulty is resolved by further decomposing the pressure gradient in (43) in terms of a genuine acoustic component, for accurate upstream modeling of acoustic waves.

4.2. Acoustic components

Following the acoustic equations (15), the flux divergence $\partial f/\partial x$ can be alternatively decomposed for arbitrary Mach numbers and corresponding dependent variables ρ, m and E as

$$\frac{\partial f}{\partial x}=\frac{\partial f^q}{\partial x}+\frac{\partial f^p}{\partial x}=\frac{\partial f^q}{\partial x}+(A^{\mathrm{a}}+A^{\mathrm{nc}})\frac{\partial q}{\partial x}. \tag{48}$$

In this decomposition, the matrices A^{a} and A^{nc} are defined as

$$A^{\mathrm{a}}\equiv\begin{pmatrix}0 & 1 & 0\\ p_\rho & 0 & p_E\\ 0 & \dfrac{c^2-p_\rho}{p_E} & 0\end{pmatrix},\qquad A^{\mathrm{nc}}\equiv\begin{pmatrix}0 & -1 & 0\\ 0 & p_m & 0\\ 0 & -\dfrac{c^2-p_\rho}{p_E} & 0\end{pmatrix}. \tag{49}$$

Heed, in particular, that no flux component of $f(q)$ exists, of which the Jacobian equals A^{a}. The eigenvalues of the matrix A^{nc} have been determined in closed form as

$$\lambda^{\mathrm{nc}}_{1,2}=0,\qquad \lambda^{\mathrm{nc}}_{3}=-cMp_Eu/|u|, \tag{50}$$

which become infinitesimal for vanishing M. The matrix A^{nc} can be termed a 'non-linear coupling' matrix, for it completes the non-linear coupling between convection and acoustics within (48) so that the two Euler eigenvalues $\lambda^E_{2,3}$ in (13) do correspond to the sum of convection and acoustic speeds. Since decomposition (48) will be used in the upstream-bias formulation for small Mach numbers only and considering that the eigenvalues in (50) vanish for these Mach numbers, no need exists to involve A^{nc} in the upstream-bias approximation of the flux Jacobian (11).

The eigenvalues of A^{a} are exactly determined in closed form as

$$\lambda^{\mathrm{a}}_{1}=0,\qquad \lambda^{\mathrm{a}}_{2,3}=\pm c. \tag{51}$$

The matrix A^{a}, therefore, can be termed the 'acoustics' matrix, for its eigenvalues, unlike (46)–(47), equal the speed of sound c for any Mach number. Despite its zero eigenvalue, A^{a} features a complete set of eigenvectors and thus possesses the similarity form

$$A^{\mathrm{a}}\equiv X\Lambda^{\mathrm{a}}X^{-1}=X\Lambda^{\mathrm{a}+}X^{-1}+X\Lambda^{\mathrm{a}-}X^{-1},\qquad \Lambda^{\mathrm{a}}=\Lambda^{\mathrm{a}+}+\Lambda^{\mathrm{a}-}, \tag{52}$$

where $\Lambda^{\mathrm{a}+}$ and $\Lambda^{\mathrm{a}-}$ respectively contain non-negative and non-positive eigenvalues. The Euler flux divergence decomposition (48) thus becomes

$$\frac{\partial f}{\partial q}=X\Lambda^{\mathrm{a}+}X^{-1}+X\Lambda^{\mathrm{a}-}X^{-1}+\frac{\partial f^q}{\partial q}+A^{\mathrm{nc}}. \tag{53}$$

Since the two acoustics matrices of the right-hand-side of this expression respectively possess non-negative and non-positive eigenvalues, a characteristics-bias approximation of these matrices involves an upstream approximation of the first matrix and a downstream approximation of the second matrix. These approximations naturally lead to the following absolute acoustics matrix upstream expression

$$|A^{a}|\frac{\partial q}{\partial x} \equiv X(\Lambda^{a+} - \Lambda^{a-})X^{-1}\frac{\partial q}{\partial x} = \begin{pmatrix} p_\rho/c & 0 & p_E/c \\ 0 & c & 0 \\ (c^2 - p_\rho)p_\rho/(cp_E) & 0 & (c^2 - p_\rho)/c \end{pmatrix}\frac{\partial q}{\partial x}. \tag{54}$$

Upon imposing the condition that the continuity and energy components in this matrix product should also satisfy the acoustic field results (18), leads to the beautifully simple result

$$|A^{a}|\frac{\partial q}{\partial x} = c\frac{\partial q}{\partial x} = cI\frac{\partial q}{\partial x}, \quad I \equiv \text{identity matrix}, \tag{55}$$

which indicates for this matrix product the equivalence of replacing $|A^{a}|$ with the matrix cI, of which all eigenvalues approach $+c$. For acoustic flows and related dependent variables E and ρ, (55) is exact. For non-acoustic flows and related arbitrary Mach number dependent variables E and ρ, (55) is approximate. This computationally advantageous approximation on the acoustics upstream bias, not on the flux divergence itself, therefore, will be used essentially in the low subsonic flow Mach number regime.

4.3. Acoustics convection characteristics flux divergence

The previous sections have shown that the flux Jacobian (11) can be equivalently expressed as

$$\frac{\partial f}{\partial q} = \begin{cases} \left[\frac{\partial f^q}{\partial q} + \beta\frac{\partial f^p}{\partial q}\right] + \left[(1-\beta)\frac{\partial f^p}{\partial q}\right] \\ X\Lambda^{a+}X^{-1} + X\Lambda^{a-}X^{-1} + \frac{\partial f^q}{\partial q} + A^{nc}, \end{cases} \tag{56}$$

where the first expression is convenient for a characteristics-bias approximation for high-subsonic and supersonic Mach numbers and the second expression is convenient for low-subsonic Mach numbers.

A flux Jacobian decomposition for all Mach numbers can thus be cast as the linear combination

$$\frac{\partial f}{\partial q} = (1-\alpha)\left\{\left[\frac{\partial f^q}{\partial q} + \beta\frac{\partial f^p}{\partial q}\right] + \left[(1-\beta)\frac{\partial f^p}{\partial q}\right]\right\} + \alpha\left\{X\Lambda^{a+}X^{-1} + X\Lambda^{a-}X^{-1} + \frac{\partial f^q}{\partial q} + A^{nc}\right\}, \tag{57}$$

with $0 \le \alpha \le 1$, which leads to the following acoustics–convection decomposition of the flux Jacobian

$$\frac{\partial f}{\partial q} = \alpha X\Lambda^{a+}X^{-1} + \alpha X\Lambda^{a-}X^{-1} + \left[\frac{\partial f^q}{\partial q} + (1-\alpha)\beta\frac{\partial f^p}{\partial q}\right] + (1-\alpha)(1-\beta)\frac{\partial f^p}{\partial q} + \alpha A^{nc}. \tag{58}$$

As mentioned in Section 4.2, an upstream approximation to the Euler flux Jacobian will be developed by establishing upstream approximations only for the first four terms in (58), where the Jacobian matrix

$$\left[\frac{\partial f^q}{\partial q} + (1+\alpha)\beta\frac{\partial f^p}{\partial q}\right]$$

is counted as one term. The reason for this coupling is that, with reference to (43), the eigenvalues of this Jacobian matrix will all keep the same algebraic sign, because $(1-\alpha)\beta \le \beta$.

One justification for this selective upstream formulation rests on the physical acoustics and convection significance of these terms. For any magnitude of both pressure and pressure gradient, the convection field uniformly carries information along streamlines; hence, the entire $\partial f^q/\partial q$ can receive an upstream-bias along one single direction. The matrices $X\Lambda^{a+}X^{-1}$ and $X\Lambda^{a-}X^{-1}$ account for the bimodal propagation of acoustic waves; these matrices are thus used for an acoustics upstream approximation for low Mach numbers. The pressure flux f^p too accounts for the bimodal propagation of acoustic waves, but in conjunction with $\partial f^q/\partial q$. As the Mach number increases from zero, a larger and larger fraction $(1-\alpha)\beta(\partial f^p/\partial q)$ of the pressure flux Jacobian can thus be upstreamed in the same direction as and along with $\partial f^q/\partial q$, while $(1-\alpha)(1-\beta)(\partial f^p/\partial q)$ is upstreamed in the opposite direction. As the Mach number increases, therefore, a smaller and smaller fraction $\alpha(X\Lambda^{a+}X^{-1}+X\Lambda^{a-}X^{-1})$ of $(X\Lambda^{a+}X^{-1}+X\Lambda^{a-}X^{-1})$ is upstreamed. The upstream-bias function α will decrease and β will increase as the Mach number increases, so as to ensure physical significance of the overall upstream-bias approximation to the first four terms in (58). The function β, in turn, depends on another function δ that leads to simpler expressions.

Given the algebraic sign of the eigenvalue set of each matrix term in (58), the associated direction cosines a_ℓ for the upstream-bias expression (28) are

$$a_1 = +1, \quad a_2 = -1, \quad a_3 = s = \mathrm{sgn}(u), \quad a_4 = -s = -\mathrm{sgn}(u), \quad a_5 = 0, \tag{59}$$

where $s = \mathrm{sgn}(u)$ denotes the algebraic sign of u. With (58), (59), approximation (55) and $\delta \equiv (1-\alpha)(2\beta-1)$, the general expression (28) leads to the acoustics–convection characteristics flux divergence

$$\frac{\partial f^{\mathrm{C}}}{\partial x} = \frac{\partial f}{\partial x} - \frac{\partial}{\partial x}\left[\varepsilon\psi\left(\alpha c I + s\frac{\partial f^q}{\partial q} + s\delta\frac{\partial f^p}{\partial q}\right)\frac{\partial q}{\partial x}\right] = \frac{\partial f}{\partial x} - \frac{\partial}{\partial x}\left[\varepsilon\psi\left(\alpha c\frac{\partial q}{\partial x} + s\frac{\partial f^q}{\partial x} + s\delta\frac{\partial f^p}{\partial x}\right)\right], \tag{60}$$

where I denotes the identity matrix of appropriate size. In particular, the coupling of an upstream approximation for $(1-\alpha)\beta(\partial f^p/\partial q)$ via a_3, with a downstream approximation for $(1-\alpha)(1-\beta)(\partial f^p/\partial q)$ via a_4 results in an overall upstream approximation of the pressure gradient, but with variable weight δ. The operation count for expression (60) is then comparable with that of an FVS formulation. The terms in this expression, furthermore, directly correspond to the physics of acoustics and convection. For low Mach numbers, $\delta = 0$ and (60) reduces to

$$\frac{\partial f^{\mathrm{C}}}{\partial x} = \frac{\partial f}{\partial x} - \frac{\partial}{\partial x}\left[\varepsilon\psi\left(\alpha c\frac{\partial q}{\partial x} + s\frac{\partial f^q}{\partial x}\right)\right], \tag{61}$$

which essentially induces only an acoustics upstream. Note that the components within f^{C} remain linearly independent of one another, which avoids the linear dependence instability in the steady low-Mach number Euler equations. For supersonic flow, $\alpha = 0$ and $\delta = 1$. Expression (60) in this case becomes

$$\frac{\partial f^{\mathrm{C}}}{\partial x} = \frac{\partial f}{\partial x} - \frac{\partial}{\partial x}\left[\varepsilon\psi\left(s\frac{\partial f}{\partial x}\right)\right], \tag{62}$$

which corresponds to an upstream approximation of the entire Euler flux divergence.

5. UPSTREAM-BIAS EIGENVALUES AND FUNCTIONS

The acoustics–convection upstream functions α and δ depend on the Mach number. They are determined by enforcing the upstream stability condition on the upstream matrix for (60). The divergence of the characteristics flux f^{C} in (60) becomes

$$\frac{\partial f^{\mathrm{C}}}{\partial x}=\frac{\partial f}{\partial x}+\frac{\partial}{\partial x}\left[\varepsilon\psi\left(\alpha cI+s\frac{\partial f^{q}}{\partial q}+s\delta\frac{\partial f^{p}}{\partial q}\right)\frac{\partial q}{\partial x}\right]. \tag{63}$$

The terms between parentheses collectively constitute the upstream-bias dissipation matrix

$$\mathscr{A}\equiv\alpha cI+s\frac{\partial f^{q}}{\partial q}+s\delta\frac{\partial f^{p}}{\partial q}. \tag{64}$$

Despite the formidable algebraic complexity of $\mathscr{A}$, all of its eigenvalues have been analytically determined exactly in closed form. Dividing through by the speed of sound c, the non-dimensional form of these eigenvalues is

$$\lambda_1=\alpha+M,\qquad \lambda_{2,3}=\alpha+\left(1+\frac{1-\delta}{2}p_E\right)M\pm\left(\left(\frac{1-\delta}{2}p_EM\right)^2+\delta\right)^{1/2}. \tag{65}$$

In order to ensure physical significance for the characteristics-bias flux within (60), hence for the upstream-bias approximation to decomposition (58), the upstream-bias functions α and δ will therefore be determined by forcing the upstream-bias eigenvalues (65) to remain positive for all Mach numbers. Following the considerations after (55), in particular, all these eigenvalues must converge to 1 for vanishing Mach number. Rather than prescribing some expressions for α and δ and accepting the resulting variations for these eigenvalues, physically reasonable expressions for these eigenvalues are instead prescribed and the corresponding functions for α and β determined.

5.1. Eigenvalue λ_3

This eigenvalue will correlate with the absolute value Euler eigenvalue $|M-1|$. As a consequence, λ_3 will vary between 1 and $1-M$ for $0\le M\le 1-\varepsilon_M$ and smoothly shift from $1-M$ to $M-1$ within the sonic transition layer $1-\varepsilon_M\le M\le 1+\varepsilon_M$, where ε_M denotes a transition-layer parameter; in this work $\varepsilon_M=\frac{1}{5}$. One expression for λ_3 that remains smooth and meets these requirements is the composite spline

$$\lambda_3(M)\equiv\begin{cases}1-M, & 0\le M\le 1-\varepsilon_M\\ \dfrac{(M-1)^2}{2\varepsilon_M}+\dfrac{\varepsilon_M}{2}, & 1-\varepsilon_M<M<1+\varepsilon_M\\ M-1, & 1+\varepsilon_M\le M\end{cases} \tag{66}$$

5.2. Eigenvalue λ_1

This eigenvalue correlates with the non-dimensional Euler eigenvalue M, but it too has to equal 1 for $M=0$; it then must coincide with M for $M>1$ and also remain greater than λ_3, as expressed through (66), for consistency with the Euler eigenvalues (13). This condition in particular implies $\lambda_1\ge\frac{1}{2}$. It thus follows that λ_1 will vary between 1 and M for $0\le M\le\frac{1}{2}+\varepsilon_M$. An expression for $\lambda_1=\lambda_1(M)$ that remains smooth and meets all of these requirements is the composite spline

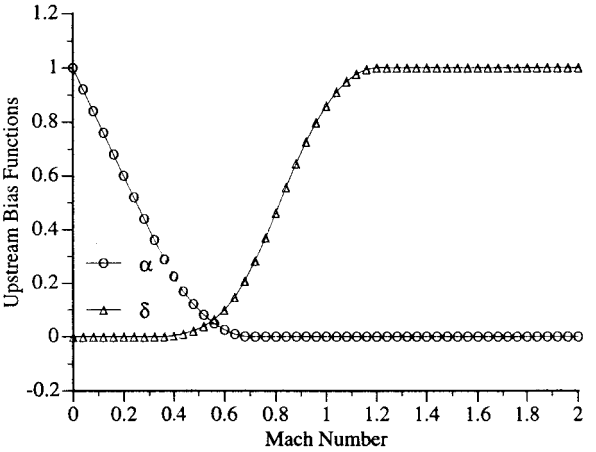

Figure 2. Upstream-bias functions.

$$\lambda_1(M) \equiv \begin{cases} 1 - M, & 0 \le M \le \frac{1}{2} - \varepsilon_M \\ \dfrac{(M-\frac{1}{2})^2}{2\varepsilon_M} + \dfrac{1+\varepsilon_M}{2}, & \frac{1}{2} - \varepsilon_M < M < \frac{1}{2} + \varepsilon_M \\ M, & \frac{1}{2} + \varepsilon_M \le M \end{cases} \tag{67}$$

5.3. Upstream-bias functions α and δ and eigenvalues

From λ_1 and λ_3 in (65), the corresponding expressions for both $\alpha = \alpha(M)$ and $\delta = \delta(M)$ have been exactly determined as

$$\alpha(M) = \lambda_1(M) - M, \qquad \delta(M) = \frac{(\lambda_1(M) - \lambda_3(M))(\lambda_1(M) - \lambda_3(M) + p_E M)}{1 + p_E M(\lambda_1(M) - \lambda_3(M))}. \tag{68}$$

The variations of the upstream-bias functions $\alpha = \alpha(M)$ and $\delta = \delta(M)$ and the corresponding eigenvalues from (65) are presented in Figures 2 and 3 respectively.

Figure 2 indicates that the upstream-bias functions as well as their slopes remain continuous for all Mach numbers, with $0 \le \alpha \le 1$, $0 \le \delta \le 1$ and $\alpha \equiv 0$ for $M > \frac{1}{2} + \varepsilon_M$, $\delta(M) \equiv 1$, for $M > 1 + \varepsilon_M$. As $\delta = \delta(M)$ rises, the upstream-bias contribution from the acoustics matrix decreases rapidly, reducing to less than 25% of its maximum at $M = 0.39$ with, therefore, concurrent reduction of the effect of the acoustic-flow formula (55). The variation of $\delta = \delta(M)$ shows that the pressure-gradient contribution to this upstream-bias formulation increases monotonically, while remaining less than 25% of its maximum, for $0 \le M \le 0.7$. When $\delta(M) \equiv 1$ for supersonic Mach numbers, the entire pressure-gradient is upstreamed with the same weight as in the convection flux, in complete agreement with the physical monoaxial wave propagation within supersonic flows.

Figure 3 shows that within $0 \le M \le 1 + \varepsilon_M$, the eigenvalues λ_1, λ_2, λ_3, smoothly approach 1 for vanishing M, indicating a physically consistent upstream-bias approximation of the acoustic equations embedded within the Euler equations. For $M > 1 + \varepsilon_M$, the eigenvalues (65) respectively coincide with the Euler flux Jacobian eigenvalues M, $M + 1$, $M - 1$, which corresponds to an upstream-bias approximation of the entire flux vector, for supersonic flows.

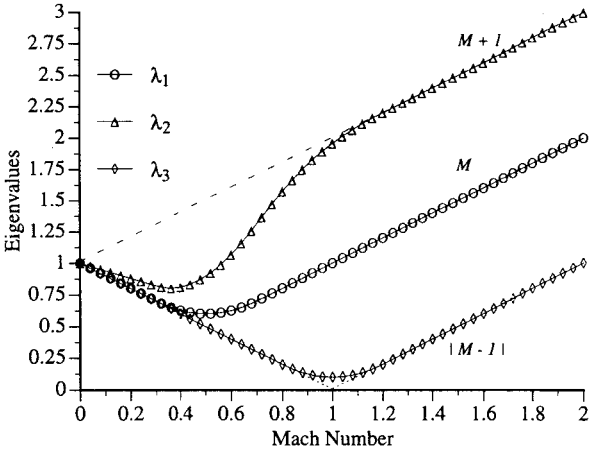

Figure 3. Upstream-bias eigenvalues.

6. FINITE ELEMENT WEAK STATEMENT

With reference to (21), the divergence (60) of the characteristics-bias flux f^{C} leads to the following characteristics-bias integral statement

$$\int_{\Omega} w\left[\frac{\partial q}{\partial t}-\phi+\frac{\partial f}{\partial x}-\frac{\partial}{\partial x}\left(\varepsilon\psi\left(\alpha c\,\frac{\partial q}{\partial x}+s\,\frac{\partial f^{q}}{\partial x}+s\delta\,\frac{\partial f^{p}}{\partial x}\right)\right)\right]\mathrm{d}\Omega=0. \tag{69}$$

An integration by parts of the upstream-bias expression then generates the weak statement

$$\int_{\Omega}\left[w\left(\frac{\partial q}{\partial t}-\phi+\frac{\partial f}{\partial x}\right)+\frac{\partial w}{\partial x}\,\varepsilon\psi\left(\alpha c\,\frac{\partial q}{\partial x}+s\,\frac{\partial f^{q}}{\partial x}+s\delta\,\frac{\partial f^{p}}{\partial x}\right)\right]\mathrm{d}\Omega=0, \tag{70}$$

where the surface integral on $\partial\Omega$ corresponding to the upstream-bias expression vanishes because of the boundary condition $\psi(x_{\partial\Omega})=0$, imposed to eliminate unnecessary boundary upstream bias. The discrete equations then result from a finite element discretization of this weak statement.

6.1. Galerkin finite element equations

The finite element weak statement [2,7,9] associated with (70) is

$$\int_{\Omega^{h}}\left[w^{h}\left(\frac{\partial q^{h}}{\partial t}-\phi^{h}+\frac{\partial f^{h}}{\partial x}\right)+\frac{\partial w^{h}}{\partial x}\,\varepsilon^{h}\psi^{h}\left(\alpha^{h}c^{h}\,\frac{\partial q^{h}}{\partial x}+s^{h}\,\frac{\partial f^{q^{h}}}{\partial x}+s^{h}\delta^{h}\,\frac{\partial f^{p^{h}}}{\partial x}\right)\right]\mathrm{d}\Omega=0, \tag{71}$$

where superscript 'h' signifies spatial discrete approximation. The approximation q^{h} exists on a partition Ω^{h}, $\Omega^{h}\subseteq\Omega$, of Ω. This partition Ω^{h} has its boundary nodes on the boundary $\partial\Omega$ of Ω and results from the union of N_e non-overlapping elements Ω_e, $\Omega^{h}=\cup_{e=1}^{N_e}\Omega_e$. For N mesh nodes within Ω^{h}, there exist clusters of 'master' elements Ω_i^{m}, each comprising only those adjacent elements that share a mesh node x_i, which implies existence of exactly N master elements. As Figure 4 shows, on each master element Ω_i^{m} the discrete test function $w^{h}\equiv w_i=w_i(x)$, $1\leq i\leq N$, will coincide with the 'pyramid' basis function with compact support on Ω_i^{m}. Such a function equals one at node x_i, zero at all other mesh nodes, and also identically vanishes both on the boundary segments of Ω_i^{m} not containing x_i, and elsewhere within the computational domain outside Ω_i^{m}.

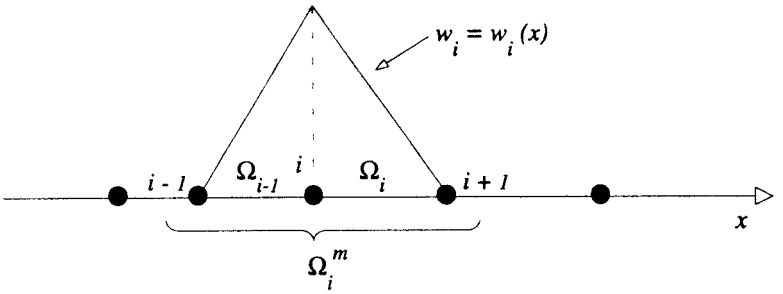

Figure 4. Master element Ω_i^{m} and test function $w_i = w_i(x)$.

Note that Ω_i^{m} represents a 'finite volume' as used in finite volume schemes, which, however, do not employ pyramid test functions. The following developments are based on a linear pyramid test function w_i, which can be expressed as

$$w_i(x) \equiv \begin{cases} \dfrac{x - x_{i-1}}{\Delta x_{i-1/2}}, & x_{i-1} \le x \le x_i \\ \dfrac{x_{i+1} - x}{\Delta x_{i+1/2}}, & x_i \le x \le x_{i+1} \end{cases} . \tag{72}$$

The discrete solution q^h at each time t assumes the form of the following linear combination

$$q^h(x, t) \equiv \sum_{j=1}^{N} w_j(x) \cdot q^h(x_j, t) \tag{73}$$

of nodal solution values and trial functions, which coincide with the test functions $w_j(x)$ for a Galerkin formulation. Similarly, the source $\phi = \phi(x, q(x, t))$ and fluxes $f = f(q(x, t))$, $f^q = f^q(q(x, t))$ and $f^p = f^p(q(x, t))$ are discretized through the group expressions

$$\phi^h(x, t) \equiv \sum_{j=1}^{N} w_j(x) \cdot \phi(x_j, q^h(x_j, t)), \qquad f^h(x, t) \equiv \sum_{j=1}^{N} w_j(x) \cdot f(q^h(x_j, t)),$$
$$f^{q^h}(x, t) \equiv \sum_{j=1}^{N} w_j(x) \cdot f^q(q^h(x_j, t)), \qquad f^{p^h}(x, t) \equiv \sum_{j=1}^{N} w_j(x) \cdot f^p(q^h(x_j, t)). \tag{74}$$

The notation for the discrete nodal variable and fluxes is then simplified as $q_j(t) \equiv q^h(x_j, t)$, $\phi_j(t) \equiv \phi^h(x_j, t)$, $f_j \equiv f^h(x_j, t)$, $f_j^q \equiv f^{q^h}(x_j, t)$, $f_j^p \equiv f^{p^h}(x_j, t)$ and expansions (73) and (74) are then inserted into (71), which yields the discrete finite element weak statement

$$\int_{\Omega^h} w_i \left[w_j \left(\frac{\mathrm{d}q_j}{\mathrm{d}t} - \phi_j \right) + \frac{\partial w_j}{\partial x} f_j \right] \mathrm{d}\Omega + \int_{\Omega^h} \frac{\partial w_i}{\partial x} \frac{\partial w_j}{\partial x} \varepsilon^h \psi^h [\alpha^h c^h q_j + s^h f_j^q + s^h \delta^h f_j^p] \, \mathrm{d}\Omega = 0, \tag{75}$$

for $1 \le i \le N$, with ε the set equal to a reference length within each element, typically a measure of the element size. While an expression like (73) for ψ^h, α^h, c^h, s^h and δ^h can be directly accommodated within (75), each of these variables in this study has been set equal to a piecewise constant for computational simplicity, one centroidal constant value per element. Since the test and trial functions w_i are prescribed functions of x, the spatial integrations in (75) are then exactly carried out, which transforms (75) into a system of ordinary differential equations (ODE) in continuum time for determining at each time level t the unknown nodal values $q^h(x_j, t)$.

For a clear comparison between traditional finite difference/volume schemes [3] and the acoustics–convection finite element algorithm (75), at any interior node 'i' of the representative grid in Figure 4, Equation (75) with $\varepsilon^h \equiv (\Delta x_{i+1/2})/2$ can be equivalently recast in difference notation as

$$\begin{aligned}
&\frac{\Delta x_{i-1/2}}{6}\left(\frac{\mathrm{d}q_{i-1}}{\mathrm{d}t}+2\frac{\mathrm{d}q_i}{\mathrm{d}t}-\phi_{i-1}-2\phi_i\right)+\frac{\Delta x_{i+1/2}}{6}\left(2\frac{\mathrm{d}q_i}{\mathrm{d}t}+\frac{\mathrm{d}q_{i+1}}{\mathrm{d}t}-2\phi_i-\phi_{i-1}\right)\\
&=-\frac{1}{2}\left[(\psi\alpha c)_{i-1/2}(q_i-q_{i-1})-(\psi\alpha c)_{i+1/2}(q_{i+1}-q_i)\right]\\
&\quad-\frac{1}{2}\left((f_i^q-f_{i-1}^q)\cdot(1+(s\psi)_{i-1/2})+(f_{i+1}^q-f_i^q)\cdot(1-(s\psi)_{i+1/2})\right)\\
&\quad-\frac{1}{2}\left((f_i^p-f_{i-1}^p)\cdot(1+(s\psi\delta)_{i-1/2})+(f_{i+1}^q-f_i^q)\cdot(1-(s\psi\delta)_{i+1/2})\right),
\end{aligned}\tag{76}$$

which uniquely couples several time derivatives at each node 'i' and features a linear combination of two-point upstream and downstream flux differences. In these finite element equations, the values of the controller ψ^h determines the combination weights of the downstream and upstream expressions, and since ψ^h remains non-negative these equations induce the appropriate upstream bias since the upstream weight $1+\psi_{i+1/2}$ always exceeds the downstream weight $1+\psi_{i-1/2}$. As a result, the finite element weak statement (75) generates consistent variable upstream-bias discrete equations that correspond to an upstream-bias discretizations for the original Euler system (1), within a compact block tridiagonal matrix statement.

For smooth solutions, these equations will still couple upstream and downstream points even for supersonic flows. The potential objection that one such algorithm would violate the physics of mono-directional wave propagation for supersonic flows is easily addressed with Courant's and Hilbert's classical developments [11] for non-linear hyperbolic systems. They in fact concluded that while waves propagate along characteristics, smooth solutions can be expanded in Taylor's series within arbitrary regions encircling any given point and along any direction radiating upstream or downstream from the point.

For a closer comparison with upwind finite volume schemes [3], the finite element equations (76) can be rearranged to generate the 'numerical flux'

$$\begin{aligned}
F_{i+1/2}\equiv\frac{f_i+f_{i+1}}{2}-\psi_{i+1/2}\Bigg[&\frac{(\alpha c)_{i+1/2}}{2}(q_{i+1}-q_i)+\frac{s_{i+1/2}}{2}(f_{i+1}^q-f_i^q)\\
&+\frac{(s\delta)_{i+1/2}}{2}(f_{i+1}^p-f_i^p)\Bigg],
\end{aligned}\tag{77}$$

which corresponds to the discrete counterpart of the characteristics-bias flux within (60). By virtue of this numerical flux, Equation (76) is recast as

$$\begin{aligned}
&\frac{\Delta x_{i-1/2}}{6}\left(\frac{\mathrm{d}q_{i-1}}{\mathrm{d}t}+2\frac{\mathrm{d}q_i}{\mathrm{d}t}-\phi_{i-1}-2\phi_i\right)+\frac{\Delta x_{i+1/2}}{6}\left(2\frac{\mathrm{d}q_i}{\mathrm{d}t}+\frac{\mathrm{d}q_{i+1}}{\mathrm{d}t}-2\phi_i-\phi_{i+1}\right)\\
&=-(F_{i+1/2}-F_{i-1/2}),
\end{aligned}\tag{78}$$

which shows that the finite element weak statement (75) naturally leads to a discretely conservative algorithm.

6.2. Boundary equations and pressure boundary condition

The integral statement (70) directly yields a set of consistent boundary differential equations, for both unconstrained boundary variables and for pressure, to enforce a pressure boundary condition at a subsonic outlet. These equations do not require any algebraic extrapolation of variables, but rather couple the time derivatives of boundary and interior node variables within the boundary cell.

For the linear elements in this study, let N and $N-1$ denote the nodes within the outlet boundary element, with N corresponding to the outlet node. For the discrete finite element equation associated with boundary node x_N, the controller ψ and test function w satisfy the conditions $\psi = 0$ and $w(x_{N-1}) = 0$, $w(x_N) = 1$.

The boundary differential equation from (75) corresponding to an outlet node becomes

$$\frac{\Delta x_{N-1/2}}{3}\left(\frac{\mathrm{d}q_{N-1}}{\mathrm{d}t} + 2\frac{\mathrm{d}q_N}{\mathrm{d}t} - \phi_{N-1} - 2\phi_N\right) = -(f_N - f_{N-1}). \tag{79}$$

This equation directly couples the time derivatives of the solution q at the adjacent boundary and interior nodes x_N and x_{N-1}. A similar equation is then obtained at an inlet, *mutatis mutandis*. Furthermore, no upstream-bias is necessary within a boundary equation, hence $\psi = 0$, because as (79) shows, this finite element boundary equation directly yields an upwind approximation for the divergence of f.

Concerning the pressure outlet boundary condition, this is naturally enforced within the surface integral that emerges in the momentum equation weak statement. The convection and pressure flux decomposition

$$f(q) = f^q(q) + f^p(q) \tag{80}$$

is first inserted into the non-discrete integral statement (70); subsequent integration by parts of the pressure gradient therein generates the weak statement

$$\int_\Omega w\left(\frac{\partial q}{\partial t} - \phi + \frac{\partial f^q}{\partial x}\right)\mathrm{d}\Omega - \int_\Omega \frac{\partial w}{\partial x} f^p \,\mathrm{d}\Omega + [w(x) f^p]_{x=x_{N-1}}^{x=x_N} = 0. \tag{81}$$

A subsequent linear finite element discretization of (81) yields

$$\frac{\Delta x_{N-1/2}}{3}\left(\frac{\mathrm{d}q_{N-1}}{\mathrm{d}t} + 2\frac{\mathrm{d}q_N}{\mathrm{d}t} - \phi_{N-1} - 2\phi_N\right) = -(f^q_N - f^q_{N-1}) - ((2f^p_{\mathrm{out}} - f^p_N) - f^p_{N-1}). \tag{82}$$

In this equation, f^p_N denotes the outlet node pressure, as calculated through the equation of state (8), whereas quite significantly, f^p_{out} can correspond to the specified outlet pressure boundary condition. This strategy for imposing an outlet pressure boundary condition remains intrinsically stable. Suppose, for instance, that some numerical perturbation forces f^p_N to decrease below the imposed f^p_{out}. In this case the outlet boundary equation (82) induces a negative time rate of change for m_N, which leads to a corresponding reduction in m_N. From the equation of state (8), this reduction then leads to an increase in f^p_N, which corresponds to a stable restoration of the imposed pressure condition. A similar conclusion on the stability of (82) is achieved by considering a perturbation increase in f^p_N. The results in Section 8 confirm the accuracy and stability of this pressure boundary condition procedure.

6.3. Discrete upstream-bias controller ψ^h

This section introduces a new upstream-bias controller ψ^h. This controller varies in the range $0 \le \psi_{\min} \le \psi^h \le \psi_{\max} \le 1$ and controls within (76) the amount of induced upstream-bias, hence

artificial diffusion. By design $\psi^h = 0$ corresponds to a classical centered discretization, hence no induced diffusion; $\psi^h = 1$, instead, corresponds to a fully upwind formulation, hence maximum diffusion.

Denote then with ψ_i the numerical value of the controller at the representative node 'i'. By analogy with (73), the discrete controller $\psi^h(x, t)$ is cast as the following linear expansion

$$\psi^h(x, t) = \sum_{j=1}^{N} w_j(x)\psi(x_j, t) = \sum_{j=1}^{N} w_j(x)\psi_j \tag{83}$$

and the centroidal evaluation of this expression within each element then yields

$$\psi_{i+1/2} = \frac{\psi_i + \psi_{i+1}}{2}. \tag{84}$$

In regions of smooth flow, ψ^h approaches $\psi_{\min}$ for a local reduction of upstream-bias diffusion; in region of discontinuous solution, ψ^h approaches $\psi_{\max}$ for an essentially non-oscillatory resolution of local discontinuities. The controller will thus correlate with a local measure φ_i of slope discontinuity.

For a smooth variation, ψ_i is expressed as a function of the measure φ_i as the composite spline

$$\psi_i \equiv \begin{cases} \psi_{\min}, & \varphi_i \le \varphi_{\mathrm{C}} \\ \psi_{\max} + \dfrac{\psi_{\max} - \psi_{\min}}{(\varphi_{\mathrm{D}} - \varphi_{\mathrm{C}})^3}, & \\ [-(\varphi_{\mathrm{D}} - 3\varphi_{\mathrm{C}})\varphi_{\mathrm{D}}^2 - 6\varphi_{\mathrm{C}}\varphi_{\mathrm{D}}\varphi_i + 3(\varphi_{\mathrm{D}} + \varphi_{\mathrm{C}})\varphi_i^2 - 2\varphi_i^3], & \varphi_{\mathrm{C}} < \varphi_i < \varphi_{\mathrm{D}} \\ \psi_{\max}, & \varphi_{\mathrm{D}} \le \varphi_i \end{cases}, \tag{85}$$

where $0 \le \varphi_i \le 1$ and the positive φ_{C} and φ_{D} respectively denote threshold continuity and discontinuity measures. Figure 5 shows the smooth variation of this type of spline controller.

The implementation of ψ^h thus requires a set of points within Ω^h where the slopes of the approximate solution are generally discontinuous. For the finite element approximation (73),

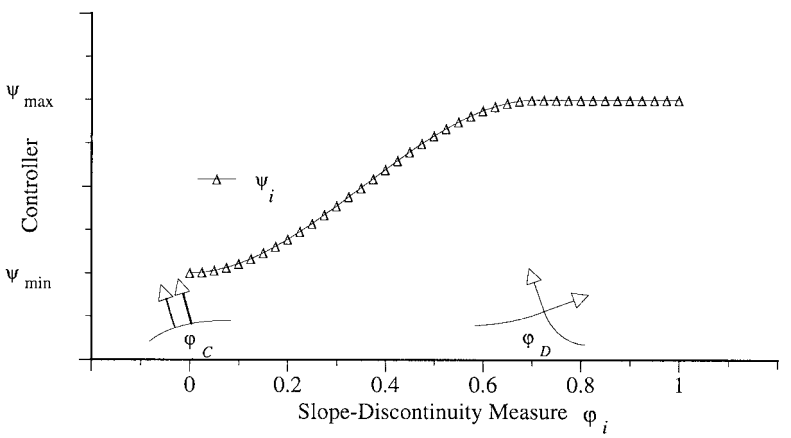

Figure 5. Variation of controller ψ_i.

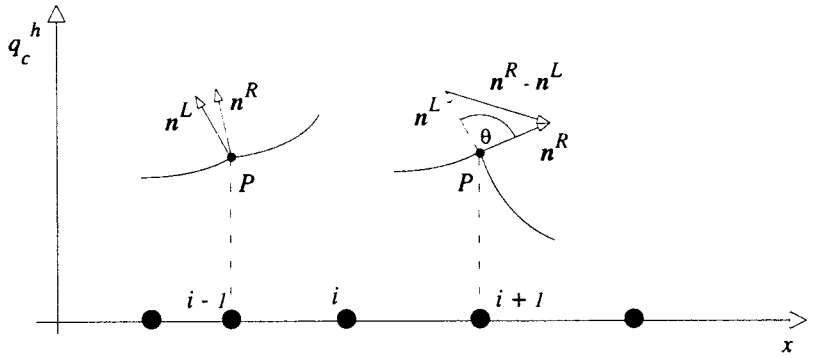

Figure 6. Slope discontinuities and local unit vectors.

this set of points is the set of finite element side nodes shared by distinct finite elements in Ω^h, for the continuous expansion (73) changes approximating polynomial from element to element, which implies that solution slopes are generally discontinuous at element side nodes. This type of slope discontinuity is depicted in Figure 6 via the local normal unit vectors $\boldsymbol{n}^{\mathrm{L}}$ and $\boldsymbol{n}^{\mathrm{R}}$ respectively to the left and right of the slope-discontinuity point P, where there exist two distinct normal unit vectors, one for each of two elements sharing the node.

With reference to Figure 6, the magnitude $\|\boldsymbol{n}^{\mathrm{R}} - \boldsymbol{n}^{\mathrm{L}}\|$ of the vector difference $\boldsymbol{n}^{\mathrm{R}} - \boldsymbol{n}^{\mathrm{L}}$ becomes proportional to a bounded measure of local-slope discontinuity. If the graph slope is continuous at P, then $\boldsymbol{n}^{\mathrm{L}}$ coincides with $\boldsymbol{n}^{\mathrm{R}}$ and $\|\boldsymbol{n}^{\mathrm{R}} - \boldsymbol{n}^{\mathrm{L}}\|$ vanishes. On the other hand, when a slope discontinuity exists at P, as shown in the figure, $\|\boldsymbol{n}^{\mathrm{R}} - \boldsymbol{n}^{\mathrm{L}}\|$ varies between 0 and 2 depending on the magnitude of the slope jump. A positive measure of slope discontinuity that vanishes for continuous slopes, remains bounded and strictly varies between 0 and 1 can thus be defined as

$$\varphi_i \equiv \frac{1}{2} \|\boldsymbol{n}^{\mathrm{R}} - \boldsymbol{n}^{\mathrm{L}}\|_{x=x_i}. \tag{86}$$

By virtue of the law of cosines, the local measure φ_i also equals

$$\varphi_i = \left(\frac{1-\cos\theta}{2}\right)^{1/2}_{x=x_i}, \tag{87}$$

where θ denotes the angle between the unit vectors in Figure 6.

With reference to Figure 7 and (87), specific numerical values for φ_{C}, φ_{D}, $\psi_{\min}$ and $\psi_{\max}$ can be easily established. At a point of solution smoothness, like point $i-1$ in the figure, $\boldsymbol{n}^{\mathrm{L}}$ will be parallel to $\boldsymbol{n}^{\mathrm{R}}$, hence $\theta = 0°$ which from (87) leads to $\varphi_{\mathrm{C}} = 0$. At a shock, instead, θ can become greater than 90°, as shown in the figure for point i. The threshold $\theta = 90°$ is thus selected for φ_{D}, which from (87) leads to $\varphi_{\mathrm{D}} = 1/\sqrt{2}$. Numerous numerical experiments with the acoustics–convection algorithm have indicated that a minimal amount of 'background' upstream bias is necessary for convergence; this finding is not surprising, since the formulation is essentially centered, hence devoid of any upstream-bias dissipation for $\psi^h = 0$. Hence, $\psi_{\min} > 0$ with typical numerical values in the range $1/4 \le \psi_{\min} \le 1/2$. Concerning $\psi_{\max}$, a relation with $\psi_{\min}$ readily follows from the requirement that in the neighborhood of a shock the maximum upstream bias can at most correspond to a fully upwind algorithm, for an essentially non-oscillatory capturing of shock waves. Hence, from (84), $\psi_{i+1/2} \le 1$ with $i+\frac{1}{2}$ denoting the centroid of a finite element (cell) that supports a shock. For a typical case of a

shock captured within at least two cells, as shown in Figure 7, (85) leads to $\psi_i = \psi_{\max}$ and $\psi_{i+1} \simeq \psi_{\min}$. From (84), therefore

$$\frac{\psi_{\max} + \psi_{\min}}{2} \leq 1 \Rightarrow \psi_{\max} \leq 2 - \psi_{\min}, \tag{88}$$

which linearly decreases as a function of increasing $\psi_{\min}$. The specific objective of letting ψ^h vary as the solution evolves is to minimize induced upstream-bias dissipation for maximum accuracy within the prescribed computational stencil. As its distinguishing design feature, the acoustics–convection upstream resolution algorithm nevertheless remains an authentic characteristics-bias formulation for any ψ^h with $\psi_{\min} \leq \psi^h \leq \psi_{\max}$.

The general expression of φ_i corresponding to a scalar component q_c^h of q^h directly derives from the finite element expansion (73), which can be expressed in synthetic implicit form as $F(q_c^h, x, t) \equiv q_c^h - q_c^h(x, t) = 0$. Hence, a normal unit vector $\boldsymbol{n}$ can be cast at each time level t as $\boldsymbol{n} \equiv \text{grad } F(q_c^h, x, t)/\|\text{grad } F\|$, where the vector operator 'grad' encompasses the dependent variable q_c^h. The expression for the corresponding φ_i at time level t and point x_i then becomes

$$\varphi_i \equiv \varphi^h(x_i, t) = \frac{1}{2}\left[\left(\frac{1}{\sqrt{1+\left(\frac{\partial q_c^{h\mathrm{R}}}{\partial x}\right)^2}} - \frac{1}{\sqrt{1+\left(\frac{\partial q_c^{h\mathrm{L}}}{\partial x}\right)^2}}\right)^2 + \left(\frac{\frac{\partial q_c^{h\mathrm{R}}}{\partial x}}{\sqrt{1+\left(\frac{\partial q_c^{h\mathrm{R}}}{\partial x}\right)^2}} - \frac{\frac{\partial q_c^{h\mathrm{L}}}{\partial x}}{\sqrt{1+\left(\frac{\partial q_c^{h\mathrm{L}}}{\partial x}\right)^2}}\right)^2\right]^{1/2}_{x=x_i}, \tag{89}$$

where the partial derivatives are determined through the finite element expansion (73), and where superscripts L and R indicate evaluation within the elements respectively to the left and right of $x = x_i$. The form of (89) at node i of a uniform grid is

$$\varphi_i = \frac{1}{2}\left[\left(\frac{\Delta x}{\sqrt{\Delta x^2 + (q_{c_{i+1}} - q_{c_i})^2}} - \frac{\Delta x}{\sqrt{\Delta x^2 + (q_{c_i} - q_{c_{i-1}})^2}}\right)^2 + \left(\frac{q_{c_{i+1}} - q_{c_i}}{\sqrt{\Delta x^2 + (q_{c_{i+1}} - q_{c_i})^2}} - \frac{q_{c_i} - q_{c_{i-1}}}{\sqrt{\Delta x^2 + (q_{c_i} - q_{c_{i-1}})^2}}\right)^2\right]^{1/2}, \tag{90}$$

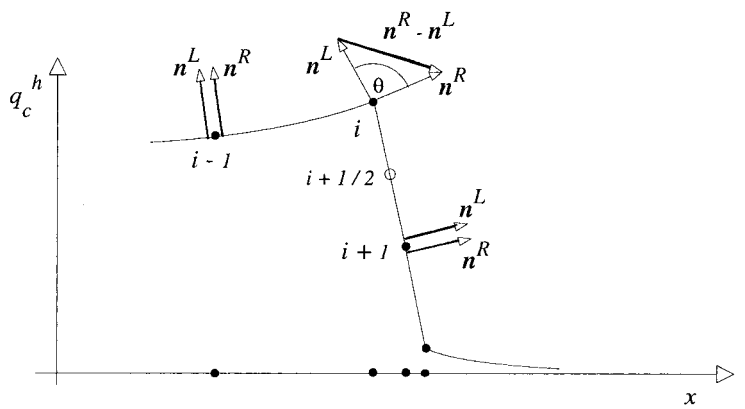

Figure 7. Local unit vectors at a shock.

Table I. Runge–Kutta coefficients

	b_1	b_2	a_{11}	a_{21}	a_{22}
IRK2	$\frac{3-\sqrt{3}}{4}$	$\frac{1+\sqrt{3}}{4}$	$\frac{3-\sqrt{3}}{6}$	$2-\sqrt{3}$	$\frac{\sqrt{3}-1}{2}$

where the denominator never vanishes. This expression, furthermore, remains bounded and differentiable for arbitrary nodal values of q_c^h. For the sole purpose of determining the order of this expression with respect to Δx, for a smooth solution over any two contiguous elements, the discrete solution values q_c, $i-1 \le j \le i+1$, over these elements, can be considered as the nodal values of a single auxiliary continuous functions $q_c(x, t)$: a Lagrangian, trigonometric or other interpolant of the q_{c_j}s over both elements. With this consideration, the Taylor's series expansion of (90) yields

$$\varphi_i = \frac{|q_c''(x_i, t)|}{1 + (q_c'(x_i, t))^2} \frac{\Delta x}{2} + \mathcal{O}(\Delta x^2) = \mathcal{K}[1 + (q_c'(x_i, t))^2]^{1/2} \frac{\Delta x}{2} + \mathcal{O}(\Delta x^2), \tag{91}$$

where superscript prime indicates differentiation with respect to x and $\mathcal{K}$ denotes the local curvature. This expansion reveals that φ_i decreases for vanishing Δx. Even for large slopes, furthermore, φ_i remains of order Δx in regions of small curvature. Only when both curvature and slope drastically rise, e.g. at a shock, will φ_i increase, which precisely corresponds to the desired behavior.

7. IMPLICIT RUNGE–KUTTA TIME INTEGRATION

The finite element equation (76) along with appropriate boundary equations and conditions, delineated in Sections 6.2 and 8, can be abridged as the non-linear ODE system

$$\mathscr{M} \frac{\mathrm{d}Q(t)}{\mathrm{d}t} = F(t, Q(t)), \tag{92}$$

where $\mathscr{M}[\mathrm{d}Q(t)/\mathrm{d}t]$ corresponds to the coupling of time derivatives in (76), and $F(t, Q(t))$ represents the remaining terms in (76). The numerical time integration of (92) in this study takes place through a new class of two-stage diagonally implicit Runge–Kutta algorithms [7] (IRK2) expressed as

$$\begin{aligned} Q_{n+1} - Q_n &= b_1 K_1 + b_2 K_2, \\ \mathscr{M} K_1 &= \Delta t \cdot F(t_n + c_1 \Delta t, Q_n + a_{11} K_1), \\ \mathscr{M} K_2 &= \Delta t \cdot F(t_n + c_2 \Delta t, Q_n + a_{21} K_1 + a_{22} K_2), \end{aligned} \tag{93}$$

where n now denotes a discrete time station and b_1, b_2, c_1, c_2, a_{11}, a_{21} and a_{22} indicate constant Runge–Kutta coefficients subject to the constraints $c_i = \Sigma_{j=1}^{i} a_{ij}$ and $\Sigma_{i=1}^{2} b_i = 1$. The coefficients for second-order accuracy are listed in Table I. With these coefficients, in particular, algorithm (93) becomes absolutely stable for arbitrary stiff non-linear dissipative ODE systems [7,12].

This algorithm is implicit because the entries in the arrays K_1 and K_2 remain coupled and are then computed by solving algebraic systems. Diagonally implicit signifies that K_1 is determined independently of K_2. Thus, given the solution Q_n at time t_n, K_1 is computed first, followed by K_2. The solution Q_{n+1} is then determined by way of the first expression in (93).

The terminal numerical solution is then determined using Newton's method, which for the implicit fully-coupled computation of the IRK2 arrays K_i, $1 \le i \le 2$, is cast as

$$\left[\mathscr{M} - a_{ii}\Delta t\left(\frac{\partial F}{\partial Q}\right)^p_{Q_i^p}\right](K_i^{p+1} - K_i^p) = \Delta t F(t_n + c_i\Delta t,\, Q_i^p) - \mathscr{M}K_i^p,$$
$$Q_i^p \equiv Q_n + a_{i1}K_1^p + a_{i2}K_2^p, \tag{94}$$

where $a_{ij} = 0$ for $j > i$, p is the iteration index and $K_1^p \equiv K_1$ for $i = 2$; for linear finite elements, the Jacobian

$$J_i(Q) \equiv \mathscr{M} - a_{ii}\Delta t\left(\frac{\partial F}{\partial Q}\right)^p_{Q_i^p} \tag{95}$$

then becomes a block tridiagonal matrix. For all the results documented in the discussion section, the initial estimate K_i^0 is set equal to the zero array, while only one iteration is executed for (94) within each time interval. In this mode, Newton's iteration becomes akin to a classical direct linearized implicit solver.

8. COMPUTATIONAL RESULTS

The computational results have validated the accuracy and essential monotonicity performance of the acoustics–convection upstream resolution algorithm for transient and steady smooth and shocked mixed subsonic/supersonic flows. The algorithm has generated essentially non-oscillatory results that automatically preserve a constant total enthalpy as well as smoothness of both enthalpy and linear momentum across steady normal shocks. These results reflect available exact solutions and numerical results independently generated [13] using van Leer's and Roe's schemes. The benchmarks in this section cover a total of five different perfect gas flows encompassing flows within: a shock tube, a convergent–divergent (DeLaval) nozzle and a steeply diverging nozzle. The corresponding spatial computational domain Ω for all the results presented is defined as: $\Omega \equiv [a, b] = [0, 1]$, uniformly discretized into 100 linear finite elements, hence $\Delta x = 0.01$. For each benchmark, the calculations proceeded with a prescribed constant maximum Courant number $C_{\max}$ defined as

$$C_{\max} \equiv \max\{|u + c|, |u - c|, c\}\,\frac{\Delta t}{\Delta x}. \tag{96}$$

Given Δx and $C_{\max}$ for each benchmark, the corresponding Δt was thus determined as

$$\Delta t = \frac{C_{\max}\Delta x}{\max\{|u + c|, |u - c|, c\}}. \tag{97}$$

As detailed in Section 6.3, the upstream-bias controller uses one scalar component of the dependent variable q. In this study, the algorithm has employed total energy E to calculate ψ.

All the solutions in these validations are presented in non-dimensional form, with density ρ, pressure p, energy E and enthalpy H made dimensionless through their respective inlet stagnation (total) values. The non-dimensional speed is obtained by way of the stagnation speed of sound divided by $\sqrt{\gamma}$. The reference speed u_r thus becomes $u_r = \sqrt{\gamma p_{\mathrm{tot_{in}}}/\rho_{\mathrm{tot_{in}}}}/\sqrt{\gamma} = \sqrt{\gamma p_{\mathrm{tot_{in}}}/\rho_{\mathrm{tot_{in}}}}$. Linear momentum is then made dimensionless through total inlet density and reference speed. For consistency with (1)–(2), however, all initial conditions and actual calculations have to employ a non-dimensional E made dimensionless through stagnation pressure.

8.1. Shock-tube flow

This benchmark consists in determining the gas flow that evolves from a rest state within a straight tube. The tube is initially divided into two chambers separated by an impermeable diaphragm placed at the midpoint on the tube axis. The non-dimensional initial conditions for the gas in each of the two chambers are

$$\rho = 1.00, \quad m = 0.00, \quad E = 2.50, \quad 0.0 \le x \le 0.5;$$
$$\rho = 0.125, \quad m = 0.00, \quad E = 0.25, \quad 0.5 < x \le 1.0. \tag{98}$$

The diaphragm ruptures at $t = 0$ and the solution corresponding to $t = 0.14152$ is sought. At this time station, the exact solution features a normal shock centered at $x = 0.75$, for each of the components of the dependent variables in q; the distribution of density ρ also develops a contact discontinuity centered at $x = 0.62$. Figure 8(a)–(c) present three density distributions as obtained with the acoustics–convection upstream resolution algorithm for $C_{\max} = 1.0$, but with a constant upstream-bias controller ψ.

The numerical values for ψ for these three solutions are $\psi = 1.0$, 0.75 and 0.5 respectively corresponding to 100%, 75% and 50% upstream bias. The figures show that a decrease in upstream-bias, hence associated artificial diffusion, corresponds to an expected increase in solution resolution. The solution in Figure 1(c), for $\psi = 0.5$, already displays correct solution features with contact discontinuity and normal shock centered at the exact locations, even though the sharp decrease in density modeling the contact discontinuity appears somewhat diffused. Note, however, that this solution remains essentially non-oscillatory without employing a fully upwind discretization with MUSCL-type extrapolation of variables.

Figures 8(d) and 9(b) present the solution generated with a variable controller ψ, with $0.25 \le \psi < 0.62$ and $C_{\max} = 1.0$. This solution remains essentially non-oscillatory throughout the computational domain. The contact discontinuity in Figure 8(d) is now resolved over about five nodes, with increased overall solution sharpness. The normal shock is captured over two nodes and the two plateaux juxtaposed the contact discontinuity remain essentially flat. Figure 9(a) presents the corresponding distribution of total energy E, which reflects the features in the density solution.

This figure also shows the associated variation of ψ, indicating that ψ remains close to its minimum over the smooth parts of the solution. Only at slope discontinuities does ψ increase, following its design features documented in Section 6.3. Therefore, ψ increases marginally, at the expansion extremities and contact discontinuity, and more markedly at the normal shock. At these locations the energy slopes abruptly change. In particular, the larger increases of ψ remain localized at the shock region, where it is precisely needed for an essentially non-oscillatory capturing of the shock. This shock is captured with ψ reaching 0.5, which corresponds to just 50% upstream bias. Away from the shock and other slope discontinuities, $\psi = 0.25$ which corresponds to a mere 25% upstream bias. This solution is therefore achieved with an essentially centered discretization, which leads to the conclusion that a uniformly fully upwind formulation is not strictly necessary within a characteristics-bias algorithm to generate an essentially sharp and non-oscillatory solution.

Figure 9(b) presents the distributions of Mach number M and associated acoustics and convection upstream-bias functions α and δ. The solution for M correlates with that for ρ and E with essentially flat plateaux and sharp normal shock. The distribution of α indicates that the acoustics upstream-bias induced via the absolute acoustics matrix (55) remains significant, at a level greater than 30%, only for $M \le 0.3$. Without this acoustics upstream bias, essential monotonicity is lost. For these Mach numbers, $\delta = 0$, which corresponds to a centered

approximation of the pressure gradient, for any ψ. For $M > 0.3$, α decreases sharply, accompanied by a corresponding rise in δ. In particular, $\alpha = 0$ for the Mach numbers corresponding to the contact discontinuity, which indicates that the absolute acoustics matrix upstream-bias term $\alpha c\, \partial q/\partial x$ plays no local role in the calculation of this discontinuity. With the calculated values of ψ, the characteristics-bias formulation for these Mach numbers is realized only through the convection and pressure gradient components intrinsic to the Euler flux divergence. The aesthetic appearance of the calculated contact discontinuity, therefore, is essentially due to the linear flux approximation employed, which only uses two nodes per cell without extrapolation of variables. As M increases towards its higher plateau, δ reaches its peak numerical value of about 0.75, which, with $\psi = 0.35$, corresponds to a mere 26.3% upstream-bias in the approximation of the pressure gradient. This level of upstream bias further decreases toward the shock, settling to a level of 15% with $\delta \simeq 0.3$ and $\psi \simeq 0.5$ at the shock.

Figure 10(a) and (b) display the associated distributions for speed and static pressure. The plateaux in these distributions remain flat and unperturbed by the density contact discontinuity, with sharp shocks captured over about two nodes.

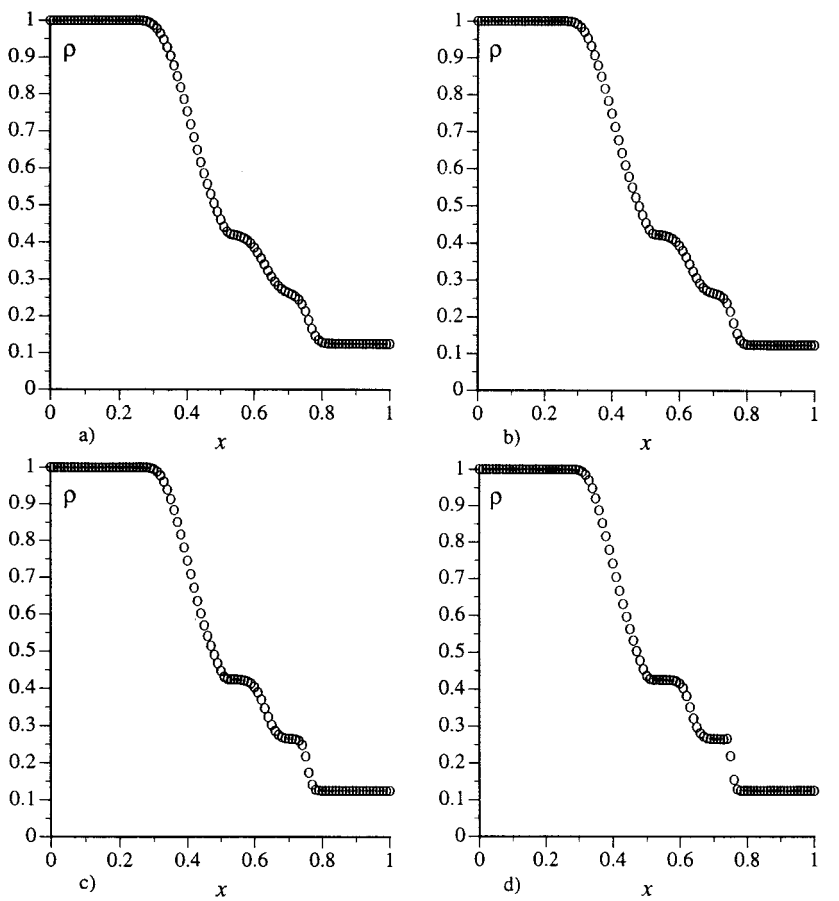

Figure 8. Density upstream-bias: (a) 100%, (b) 75%, (c) 50%, (d) 25%–50% controlled.

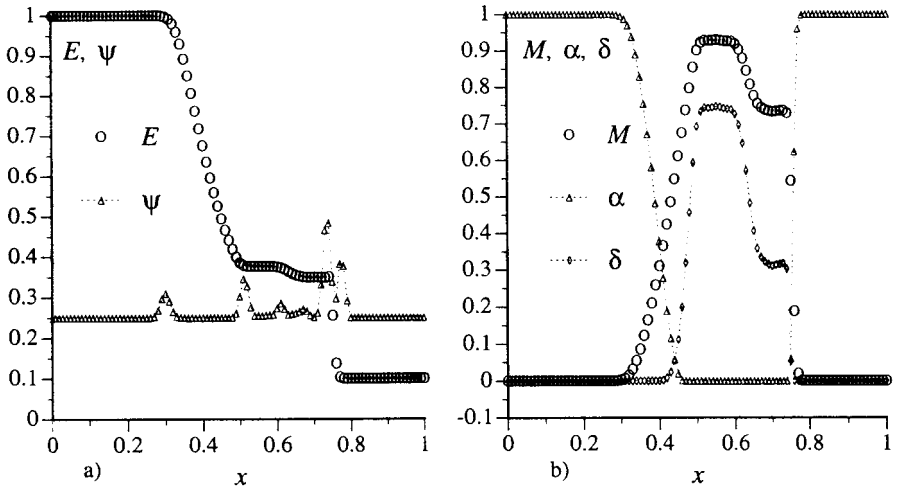

Figure 9. Controlled upstream: (a) energy and controller, (b) Mach number, α and δ.

8.2. Flows in a converging–diverging nozzle

These benchmarks test the capability of the algorithm to calculate steady isentropic and shocked flows that contain a low-Mach number subsonic region. The nozzle cross-section area distribution remains continuous with continuous slopes, but contains a discontinuous throat curvature [13], as shown in Figure 11. This feature will induce a nozzle throat discontinuous curvature in the flow variables even for an isentropic flow, which makes this benchmark particularly useful to assess algorithm resolution.

The nozzle area ratio distribution for these benchmarks is

$$\frac{A(x)}{A_{*\text{in}}} = \begin{cases} 1.75 - 0.75\cos(\pi(2x-1)), & 0 \le x \le \frac{1}{2} \\ 1.25 - 0.25\cos(\pi(2x-1)), & \frac{1}{2} \le x \le 1 \end{cases}, \tag{99}$$

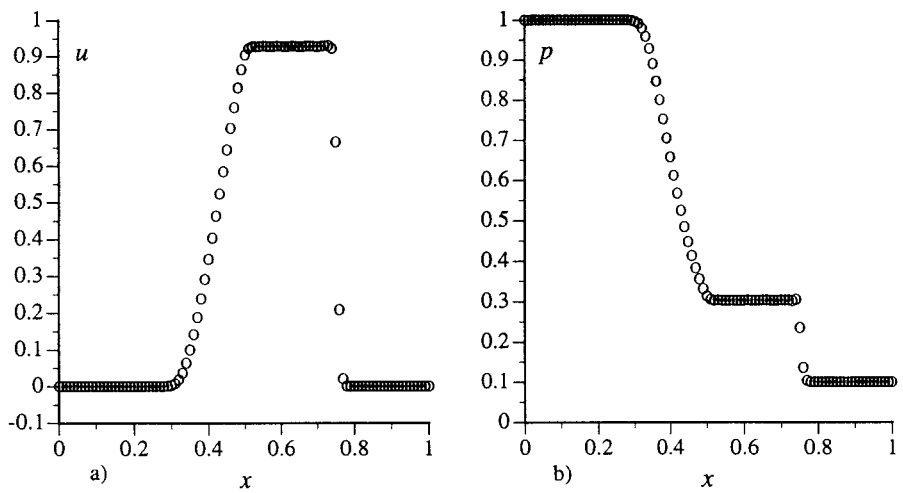

Figure 10. Controlled upstream: (a) speed, (b) pressure.

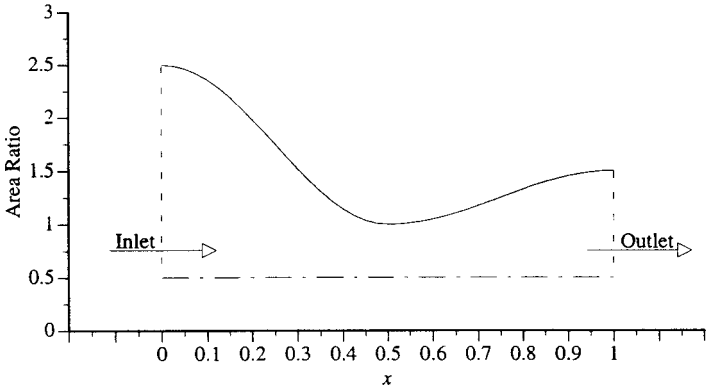

Figure 11. Variation of area ratio $A(x)/A_*$.

with

$$\frac{A(0)}{A_{*\text{in}}} = 2.5, \qquad \frac{A(1)}{A_{*\text{in}}} = 1.5. \tag{100}$$

The initial conditions for the gas correspond to an $M = 0.23954$ uniform state, leading to the following initial numerical values for ρ, m and E throughout the nozzle

$$\rho = 0.97188, \quad m = 0.27389, \quad E = 2.44072. \tag{101}$$

The inlet remains subsonic and the physically admissible boundary conditions specified at the inlet are constant Dirichlet conditions on density ρ and total energy E, equal to the initial conditions. An outlet boundary condition is also imposed at a subsonic outlet, as discussed in Section 6.2.

8.2.1. Isentropic supersonic flow. For the given initial conditions, the outlet is temporarily subsonic and a pressure boundary condition is imposed. This corresponds to the jump decrease in static pressure: $p/p_{\text{tot}_{\text{in}}} = 0.16017$, pertinent to the terminal steady state outlet supersonic Mach number $M = 1.85413$. The algorithm monitors the outlet Mach number during the calculations and when it exceeds 1, the outlet pressure boundary condition is released, allowing the calculations to proceed toward a steady state without any further outlet boundary condition.

Figure 12(a) and (b) present the convergence rate and steady state speed and Figure 13(a) and (b) show the distributions of density, linear momentum, pressure and enthalpy.

The acoustic–convection upstream resolution algorithm generated a steady state with a reduction of the maximum residual by 13 orders of magnitude, down to machine zero in about 25 time steps with $C_{\max} = 400$. The calculated speed reflects the exact solution, indicated with a solid line. This distribution clearly shows the sonic point curvature discontinuity, which remains devoid of any unphysical expansion shock and follows the exact solution.

The distributions of density, linear momentum, pressure and enthalpy in Figure 13(a) and (b) also reflect the corresponding exact solutions with the curvature discontinuity clearly resolved. The algorithm has also correctly held constant the computed enthalpy, which satisfies the steady adiabatic-flow constant enthalpy condition. Figure 14(a) presents the distributions of total energy E, which visually coincides with the exact solution, and upstream-bias controller ψ, with $0.25 \leq \psi < 1.0$. Since the solution does not contain any shock, ψ varies

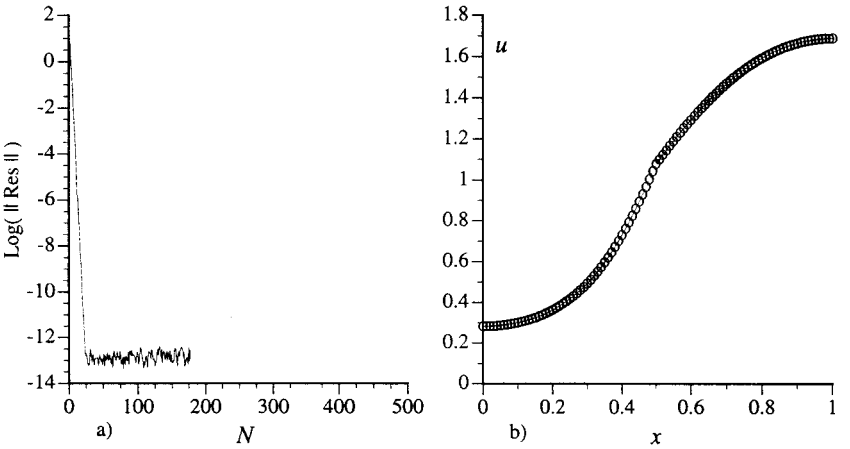

Figure 12. Isentropic flow: (a) convergence rate, (b) speed.

modestly, with $\psi \simeq 0.25$ for this steady state, which corresponds to a 25% upstream-bias. The obvious location where ψ increases mildly to $\psi = 0.275$, is at the curvature discontinuity, which correlates with the theoretical finding (91).

Figure 14(b) presents the distribution of Mach number M, which also reflects the exact solution, and the corresponding distributions of the acoustics and pressure gradient upstream-bias functions α and δ. According to these distributions, the acoustics upstream-bias vanishes for $M \geq 0.7$ and is present with decreasing weight only in the subsonic region of the flow, for $M < 0.7$. For these Mach numbers, $\delta \simeq 0$, which corresponds to a centered approximation of the pressure gradient for any ψ. For increasing M beyond $M = 0.7$, δ rises briskly, which corresponds to a rapid upstream-bias growth in the approximation of the pressure gradient. For $M > 1$, $\delta = 1$, which makes the pressure gradient upstream-bias weight equal to that on the convection divergence.

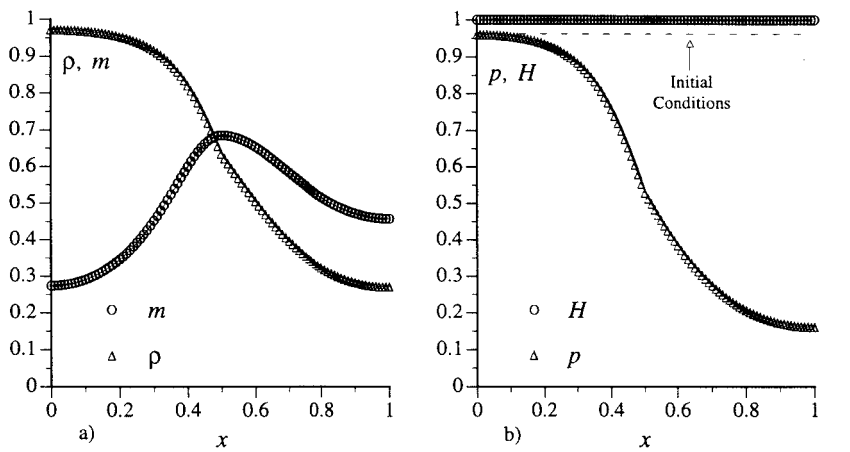

Figure 13. Isentropic flow: (a) density and momentum, (b) pressure and enthalpy.

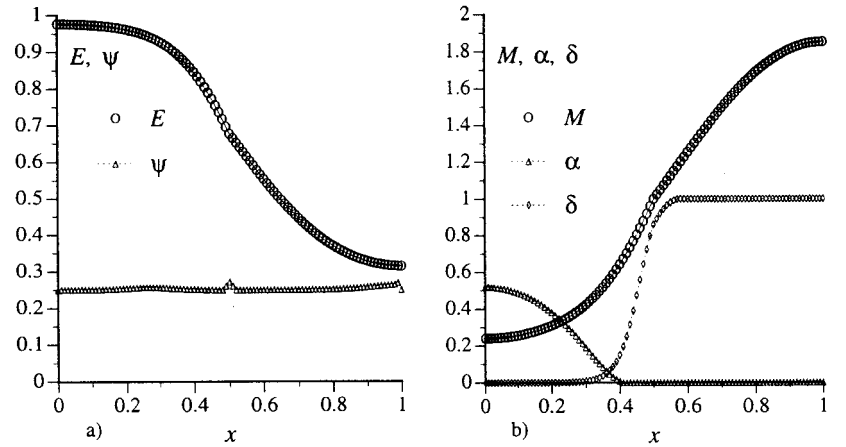

Figure 14. Isentropic flow: (a) energy and controller, (b) Mach number, α and δ.

8.2.2. Flow with embedded normal shock. A normal shock wave features in this steady flow as a result of the subsonic outlet pressure boundary condition $p/p_{\mathrm{tot}_{\mathrm{in}}} = 0.84$, imposed as an impulsive step decrease from the initial conditions and for the entire flow evolution toward steady state. The theoretical solution places the normal shock at the area ratio $A_s/A_{*\mathrm{in}} = 1.09896$, which corresponds to the interior of the finite element with node co-ordinates $x = 0.64$ and $x = 0.65$, within the computational domain. The exact shock Mach numbers are $M_{\mathrm{sup}} = 1.36989$ and $M_{\mathrm{sub}} = 0.75274$, which lead to the stagnation pressure and critical area ratios $p_{\mathrm{tot}_{\mathrm{out}}}/p_{\mathrm{tot}_{\mathrm{in}}} = A_{*\mathrm{in}}/A_{*\mathrm{out}} = 0.96537$. The associated outlet area ratio and Mach number are $A_{\mathrm{out}}/A_{*\mathrm{in}} = 1.5$, $M_{\mathrm{out}} = 0.45025$.

Figure 15(a) and (b) present the convergence rate and steady state speed. The steady state was achieved in about 25 time steps, for a total of about 50 IRK cycles, with $C_{\max} = 400$ and a reduction of the maximum residual by 13 orders of magnitude, down to machine zero. In comparison, Reference [13] reports that a steady state for the same problem was achieved with a minimum of 175 cycles. The calculated speed reflects the exact solution, indicated with a

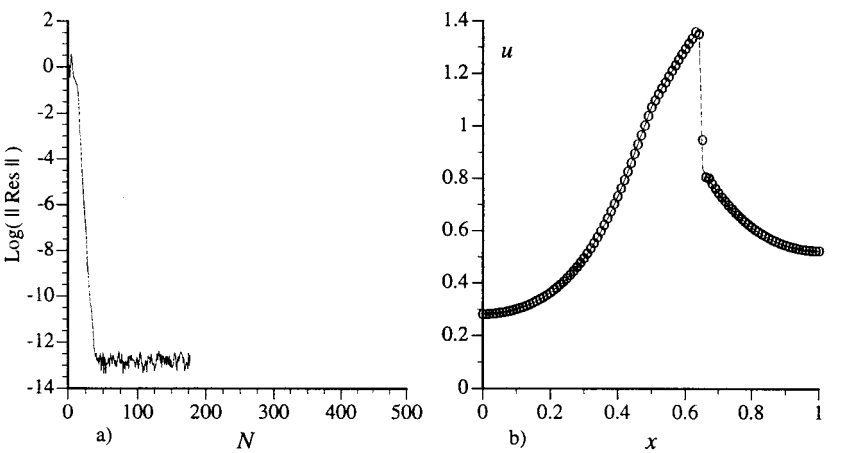

Figure 15. Shocked flow: (a) convergence rate, (b) speed.

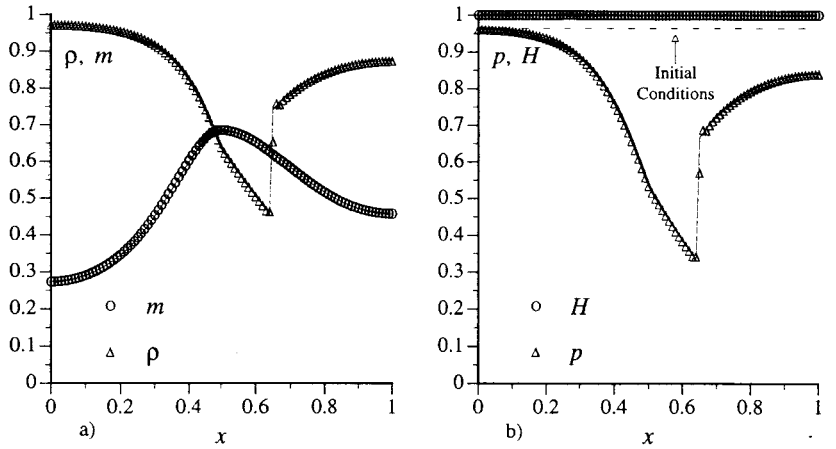

Figure 16. Shocked flow: (a) density and momentum, (b) pressure and enthalpy.

solid line. This distribution clearly shows the sonic point curvature discontinuity, as well as the normal shock which is captured at the correct location, within about two elements with a mild shock foot undershoot, similar to that in Reference [13].

The distributions of static density and pressure in Figure 16(a) and (b) also reflect the corresponding exact solutions with the curvature discontinuity clearly resolved and normal shock sharply captured over only one internal node with slight shock foot overshoots. Significantly, the algorithm has correctly generated continuous distributions for both linear momentum m and enthalpy H across the normal shock, without any shock bump. Furthermore, the computed H remains accurately constant, as has to be the case for a steady adiabatic flow.

Figure 17(a) presents the distributions of total energy E, which visually coincides with the exact solution in solid line, and upstream bias controller ψ, with $0.5 \leq \psi < 1.0$. The controller remains essentially constant over smooth solution regions, with $\psi = 0.5$, which corresponds to a 50% upstream-bias. At the shock, ψ rapidly rises, reaching a $\psi \simeq 0.9$ extremum, which induces a 90% upstream-bias. This increase in ψ appears sudden; presumably a slightly milder variation of ψ at the shock could obviate the modest overshoots in ρ, p and E. On the other hand, the algorithm succeeds in focusing an increased level of upstream-bias, hence artificial dissipation at the shock region only, precisely where required for an essentially sharp and non-oscillatory solution.

Figure 17(b) presents the distribution of Mach number M, which also reflects the exact solution, and the corresponding distributions of the acoustics and pressure-gradient upstream-bias functions α and δ. According to these distributions, the acoustics upstream-bias is present, with decreasing weight, only within the inlet and outlet subsonic regions of the flow. This type of upstream-bias vanishes in the supersonic region, including the normal shock, hence it plays no local role in the computation of the shock. Shock resolution, therefore, is entirely due to the convection and pressure gradient upstream biases, which occur with the same weight at the supersonic side of the shock, where $\delta = 1$. As M falls across the shock, so does δ, which indicates that the upstream bias in the approximation of the pressure gradient quickly decreases, leading to an essentially centered approximation of this gradient towards the outlet. For all the distributions computed for this benchmark, the outlet variations remain smooth and undistorted; in particular, the calculated outlet pressure coincides with the imposed

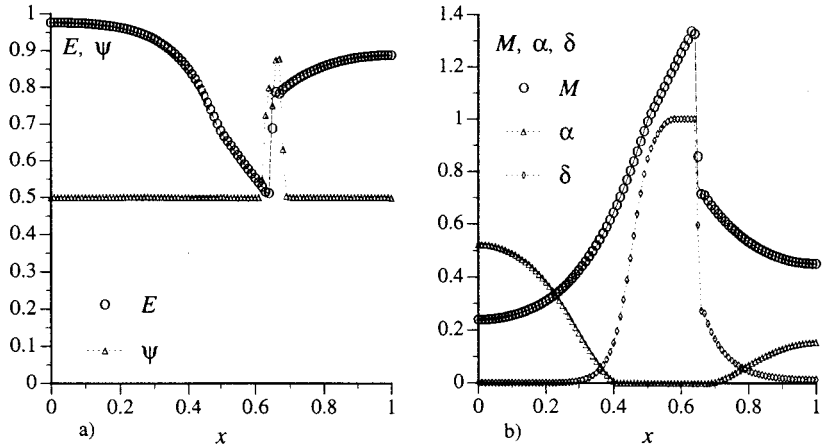

Figure 17. Shocked flow: (a) energy and controller, (b) Mach number, α and δ.

pressure boundary conditions, which reflects favorably on the surface integral pressure enforcement strategy delineated in Section 6.2.

8.3. Flows in a diverging nozzle

These benchmarks examine the capability of the algorithm to calculate steady isentropic and shocked flows that involve a high-Mach number supersonic region. The nozzle cross-section area distribution features a steep increase in the diverging region [13], as shown in Figure 18, which makes it challenging numerically to compute a non-oscillatory shock located in such a region.

The nozzle area ratio distribution for these benchmarks is

$$\frac{A(x)}{A_{*\text{in}}} = a + b \tanh(8x - 4), \tag{102}$$

with

$$a = 1.39777, \quad b = 0.34760, \tag{103}$$

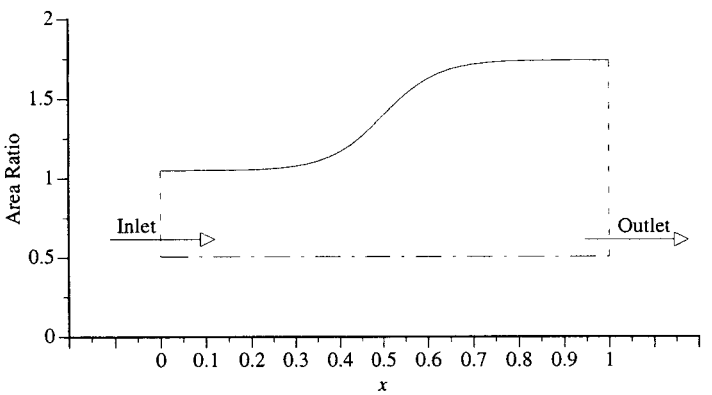

Figure 18. Variation of area ratio $A(x)/A_*$.

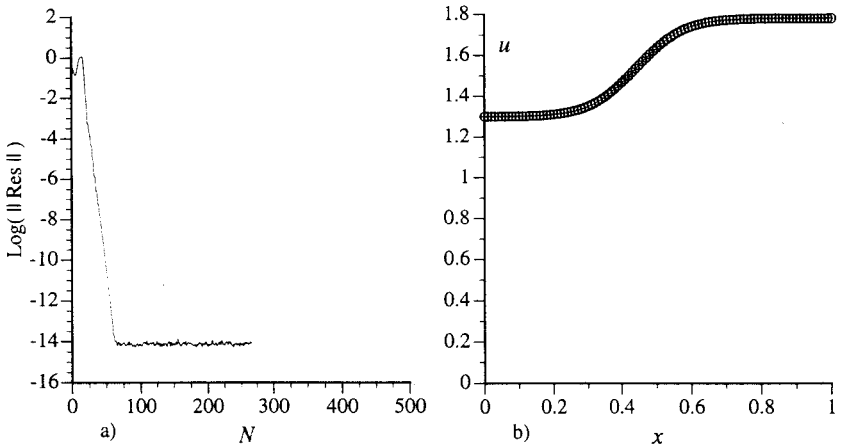

Figure 19. Isentropic flow: (a) convergence rate, (b) speed.

and

$$\frac{A(0)}{A_{*\text{in}}} = 1.05041, \quad \frac{A(1)}{A_{*\text{in}}} = 1.74514. \tag{104}$$

The initial conditions for the gas correspond to an $M = 1.26$ uniform supersonic state, which leads to the following initial state throughout the nozzle

$$\rho = 0.50189, \quad m = 0.65187, \quad E = 1.37567. \tag{105}$$

The inlet flow is constrained supersonic at $M = 1.26$; Dirichlet boundary conditions are thus enforced on density ρ, linear momentum m and total energy E. An outlet pressure boundary condition is also imposed for the simulation of a shocked flow.

8.3.1. Isentropic supersonic flow. For the given initial condition, the outlet is already supersonic, hence no boundary conditions are enforced at the outlet. The solution of the flow from the initial conditions is thus entirely driven by the area source term in the governing Euler equations (1) and (2).

Figure 19(a) and (b) presents the convergence rate and steady state speed. The acoustics–convection upstream resolution algorithm generated a steady state with a reduction of the maximum residual by 14 orders of magnitude, down to machine zero in about 60 time steps with $C_{\max} = 800$. The calculated speed reflects the exact solution, indicated with a solid line. This distribution clearly shows the rapid increase that is triggered by the drastic nozzle enlargement.

The distributions of density, linear momentum, pressure and enthalpy in Figure 20(a) and (b) also mirror the corresponding exact solutions, with swift expansions clearly resolved. The algorithm has also correctly held constant the computed enthalpy, which satisfies the steady adiabatic flow constant enthalpy condition. Figure 21(a) presents the distributions of total energy E, which remains indistinguishable from the exact solution, and upstream bias controller ψ, with $0.25 \leq \psi < 1.0$. Since the solution is smooth, ψ stays virtually constant with $\psi \simeq 0.25$ for this steady state, which corresponds to a 25% upstream bias.

Figure 21(b) presents the distribution of Mach number M, which also agrees with the exact solution. and the variations of acoustics and pressure gradient upstream-bias functions α and δ.

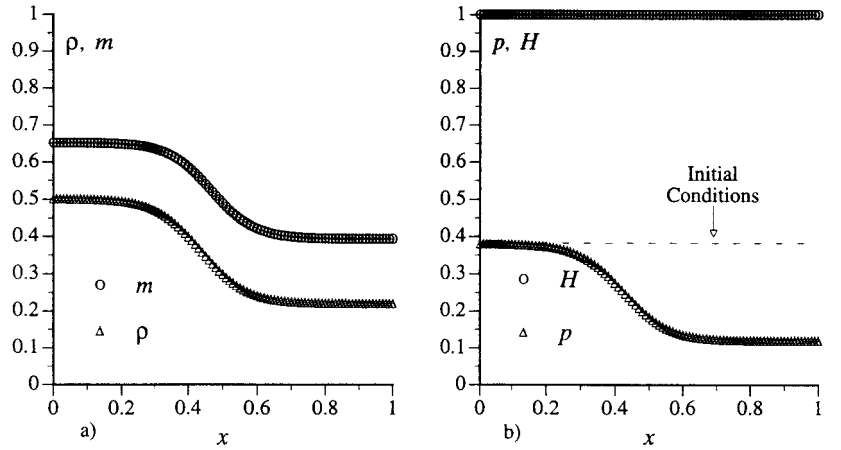

Figure 20. Isentropic flow: (a) density and momentum, (b) pressure and enthalpy.

For a supersonic flow, $\alpha \equiv 0$ and $\delta \equiv 1$. No acoustic matrix upstream-bias is thus present in this solution and the entire flux divergence receives a uniform upstream-bias approximation.

8.3.2. Flow with embedded normal shock. A normal shock wave features in this steady flow as a result of the subsonic outlet pressure boundary condition $p/p_{\mathrm{tot}_{\mathrm{in}}} = 0.746$, imposed as an impulsive step decrease from the initial conditions, for the entire flow evolution toward steady state. The theoretical solution places the normal shock at the area ratio $A_s/A_{*\mathrm{in}} = 1.35016$, which corresponds to the interior of the finite element with node co-ordinates $x = 0.48$ and $x = 0.49$, within the computational domain. The exact shock Mach numbers are $M_{\mathrm{sup}} = 1.71319$ and $M_{\mathrm{sub}} = 0.63717$, which lead to the stagnation pressure and critical area ratios $p_{\mathrm{tot}_{\mathrm{out}}}/p_{\mathrm{tot}_{\mathrm{in}}} = A_{*\mathrm{in}}/A_{*\mathrm{out}} = 0.85022$. The associated outlet area ratio and Mach number are $A_{\mathrm{out}}/A_{*\mathrm{in}} = 1.74514$, $M_{\mathrm{out}} = 0.43629$.

Figures 22(a) and (b) present the convergence rate and steady state speed. The algorithm is certainly capable of driving the maximum residual down to machine zero, with a total residual reduction by 14 orders of magnitude, with $C_{\max} = 12$; a residual reduction by six orders of

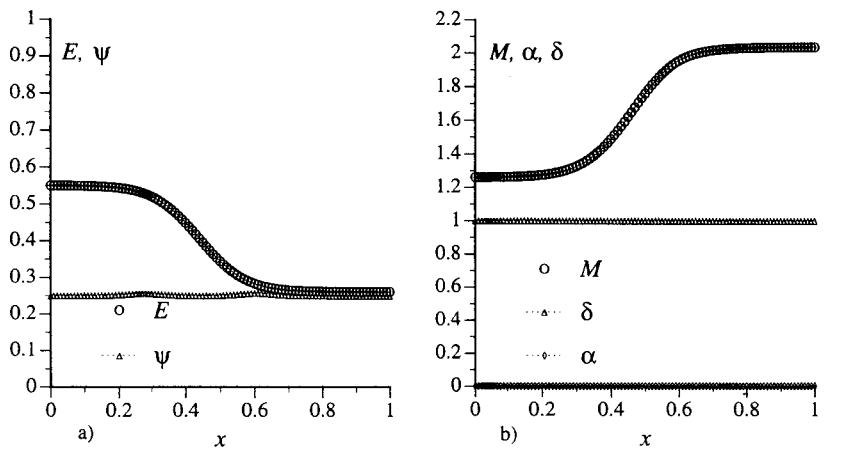

Figure 21. Isentropic flow: (a) energy and controller, (b) Mach number, α and δ.

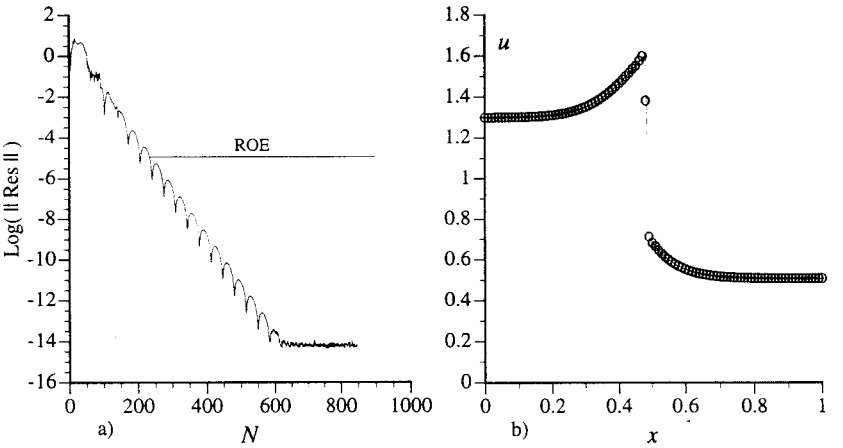

Figure 22. Shocked flow: (a) convergence rate, (b) speed.

magnitude occurs within about 250 time steps. Other initial conditions, closer to the steady state, would presumably lead to faster convergence. These results, however, compare favorably with those in Reference [13], which reports lack of convergence with Roe's algorithm for this benchmark and with a similar computational solution. This comparison rests on the observation that the acoustics–convection upstream resolution algorithm is not a purely flux vector splitting algorithm, but it also uses, like Roe's algorithm, a Riemann solver, although applied to the acoustics equations. The calculated speed reflects the exact solution, indicated with a solid line, and clearly shows the expected rapid rise preceding the shock as well as an excellent calculated normal shock, captured over only one node.

The distributions of static density and pressure in Figure 23(a) and (b) also reflect the corresponding exact solutions, with rapid changes in these two variables clearly resolved and normal shock again sharply captured over one internal node. In harmony with the previous benchmark results, also for this problem has the algorithm correctly generated continuous distributions for both linear momentum m and enthalpy H across the normal shock, without any shock bump. Furthermore, the computed H remains again constant, as has to be the case for a steady adiabatic flow.

Figure 24(a) presents the distributions of total energy E, which visually coincides with the exact solution in solid line, and upstream bias controller ψ, with $0.4 \leq \psi < 1.5$. The controller remains essentially constant over smooth solution regions, with $\psi = 0.4$, which corresponds to a 40% upstream-bias. At the shock, ψ rapidly rises and reaches a $\psi \simeq 0.96$ extremum, which induces a 96% upstream-bias. This increase in ψ appears less sudden at its inception than that in Figure 17(a), which reinforces the conjecture that a relatively smooth increase of ψ at a normal shock can obviate modest shock overshoots. No overshoots are present in this solution, and as Figure 24(a) bears out the algorithm succeeds in focusing an increased level of upstream-bias, hence artificial dissipation, at the shock region only, precisely where required for an essentially sharp and non-oscillatory solution. Figure 24(b) presents the distribution of Mach number M, which also reflects the exact solution, and the corresponding distributions of the acoustics and pressure gradient upstream-bias functions α and δ. According to these distributions, the acoustics upstream-bias is present only in the outlet subsonic regions of the flow. This type of upstream-bias vanishes in the supersonic region, including the normal shock, hence it plays no local role in the computation of the shock. Also in this case, therefore, is

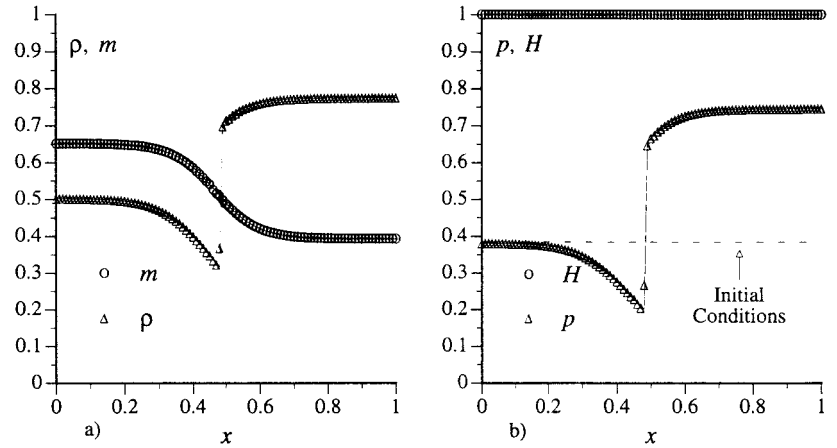

Figure 23. Shocked flow: (a) density and momentum, (b) pressure and enthalpy.

shock resolution entirely due to the convection and pressure gradient upstream biases, which occur with the same weight at the supersonic side of the shock, where $\delta = 1$. As M falls across the shock, so does δ, which indicates that the upstream bias in the approximation of the pressure gradient quickly decreases, leading to an essentially centered approximation of this gradient towards the outlet. Also for all the distributions computed for this benchmark are the outlet variations smooth and undistorted; in particular the calculated outlet pressure coincides with the imposed pressure boundary conditions, which again reflects favorably on the surface integral pressure enforcement strategy.

9. CONCLUDING REMARKS

The acoustics–convection upstream resolution algorithm rests on the physics and mathematics of acoustics and convection. It introduces a decomposition of the flux vector Jacobian into

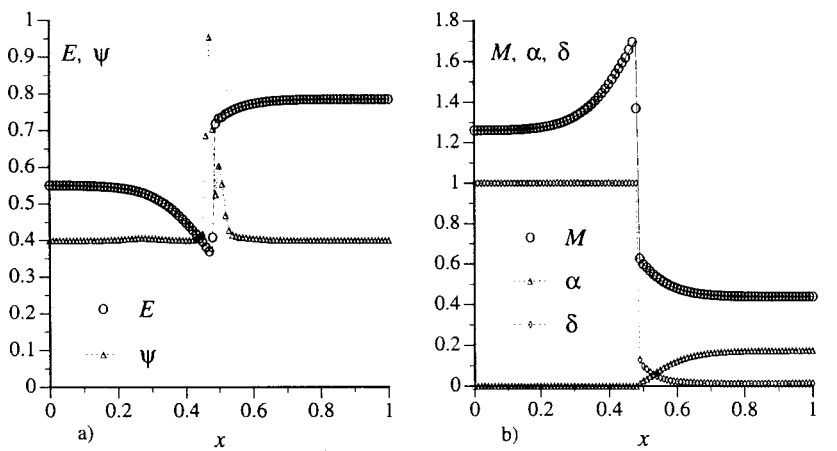

Figure 24. Shocked flow: (a) energy and controller, (b) Mach number, α and δ.

acoustics and convection matrix components, for general equilibrium equations of state, and generates the upstream-bias at the differential equation level before any discrete approximation. This formulation generates a characteristics-bias flux that generalizes in the continuum the traditional upwind scheme numerical fluxes.

A natural finite element discretization of the characteristics-bias flux generates an essentially centered approximation of the Euler flux divergence, in the form of a non-linear combination of upstream diffusive and downstream anti-diffusive flux differences, with greater bias on the upstream diffusive flux difference. The algorithm induces this upstream-bias and associated artificial diffusion mostly locally in regions of solution discontinuities, whereas it decreases the upstream-bias in regions of solution smoothness. This solution-driven variable upstream-bias thus minimizes artificial dissipation via an upstream-bias controller that depends on the jumps of solution slopes. The study in this paper has implemented the algorithm using a linear approximation of fluxes within two-noded cells, without any MUSCL-type local extrapolation of variables.

The computational results have validated accuracy and essential monotonicity performance of the acoustics–convection upstream resolution algorithm for transient and steady smooth and shocked flows. The algorithm generates essentially non-oscillatory solutions and automatically preserves a constant enthalpy as well as smoothness of both enthalpy and mass flux across steady normal shocks. These results have also validated an intrinsically stable pressure boundary condition procedure at a subsonic outlet. This procedure directly enforces the outlet pressure within the surface integral that emerges in the momentum equation weak statement. The computed solutions at nozzle outlets remain smooth and undistorted and mirror the exact reference solutions, which bears out the reliability of this pressure boundary condition.

According to the solution-driven numerical values of the upstream-bias controller, the computed smooth and shocked solutions resulted from a mostly centered discretization. This finding indicates that a uniformly fully upwind formulation is not strictly necessary within a characteristics-bias algorithm to generate essentially sharp and non-oscillatory solutions. The algorithm, therefore, succeeds in both reducing artificial dissipation in regions of smooth flow, for higher accuracy, and focusing an adequate level of upstream-bias, hence artificial dissipation, at the shock regions, only, precisely where required for stability and sharp shock capturing.

The computational results agree with the reference solutions, with curvature discontinuities exactly calculated and sharp normal shocks captured over one or two points. The finite element acoustics–convection upstream resolution algorithm, therefore, delivers solutions that are as sharp and non-oscillatory as those generated by local extrapolation flux vector and flux difference splitting schemes [13]. This characteristics-bias algorithm, however, admits a straightforward implicit implementation, features a computational simplicity that parallels a traditional centered discretization, and rationally decreases superfluous artificial diffusion. Ongoing work is completing an intrinsically multi-dimensional and infinite directional acoustics–convection algorithm, to be detailed in a future paper.

ACKNOWLEDGMENTS

The research in this paper has been partly supported by the US Army Research Office (ARO) under grant number DAAH04-96-1-0095. The author is especially grateful to Dr Tom Doligalski, program manager, for this ARO support.

REFERENCES

1. T.J.R. Hughes, 'Recent progress in the development and understanding of SUPG methods with special reference to the compressible Euler and Navier–Stokes equations', *Int. J. Numer. Methods Fluids*, **7**, 11 (1987).
2. A.J. Baker and J.W. Kim, 'A Taylor weak statement algorithm for hyperbolic conservation laws', *Int. J. Numer. Methods Fluids*, **7**, 489–520 (1987).
3. C. Hirsch, *Numerical Computation of Internal and External Flows*, vols. 1 and 2, Wiley, New York, 1991.
4. P.L. Roe, 'Approximate Riemann solvers, parameter vectors, and difference schemes', *J. Comput. Phys.*, **43**, 357–372 (1981).
5. W. Coirer and B. van Leer, 'Numerical flux formulas for the Euler and Navier–Stokes equations: II. Progress in flux-vector splitting', *AIAA-91-1566*, 1991.
6. M.-S. Liou and C.J. Steffen, 'A new flux splitting scheme', *J. Comput. Phys.*, **107**, 23–29 (1993).
7. G.S. Iannelli and A.J. Baker, 'An intrinisically N-dimensional generalized flux vector splitting implicit finite element Euler algorithm', *AIAA 91-0123*, *29th Aerospace Sciences Meeting*, Reno, NV, 1991.
8. W.G. Vincenti and C.H. Kruger, Jr., *Introduction to Physical Gas Dynamics*, Wiley, New York, 1965.
9. G.S. Iannelli, 'A CFD Euler solver from a physical acoustics–convection flux divergence decomposition', *US Army Technical Report*, *ARO DAAH04-96-1-0095*, 1997.
10. R.A. Horn, C.R. Johnson, *Matrix Analysis*, Cambridge University Press, Cambridge, 1991.
11. R. Courant and D. Hilbert, *Methods of Mathematical Physics*, Wiley, New York, 1989.
12. K. Dekker and J.G. Verwer, *Stability of Runge–Kutta Methods for Stiff Non-Linear Differential Equations*, Elsevier Publishers, Amsterdam, 1984.
13. M.-S. Liou and B. van Leer, 'Choice of implicit and explicit operators for the upwind differencing method', *AIAA 88-0624*, *26th Aerospace Sciences Meeting*, Reno, NV, 1988.

